Cell

ER-to-Golgi protein delivery through an interwoven, tubular network extending from ER

Graphical abstract

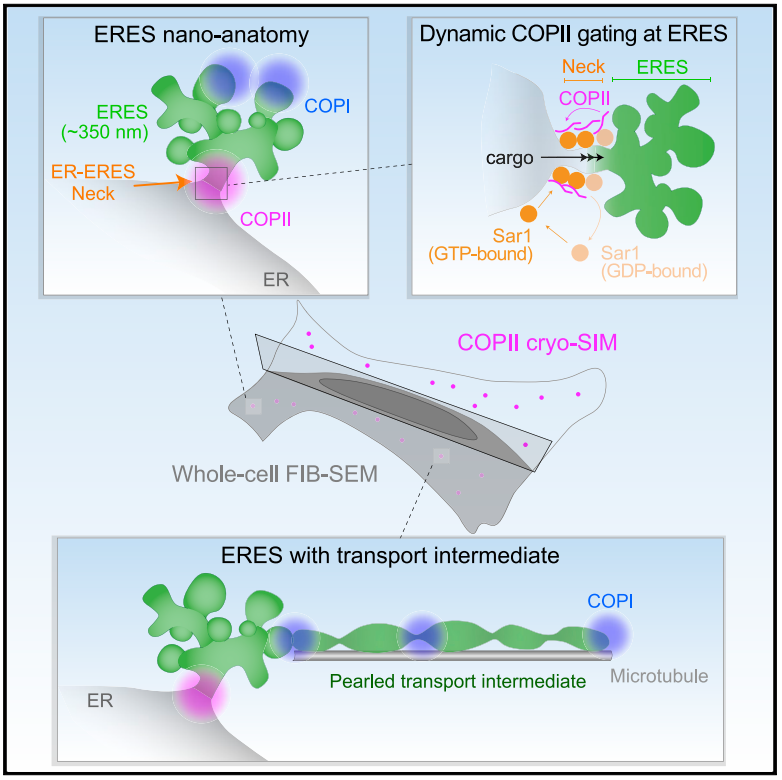

Highlights

- Isotropic nano-anatomy of early secretory compartments in intact mammalian cells
- ERESs are tangled tubule networks connected to and exchanging content with the ER
- COPII and COPI act sequentially at ERESs for ER-to-Golgi cargo movement
- ERESs derive pearled membrane vessels moving along microtubules for Golgi delivery

Authors

Aubrey V. Weigel, Chi-Lun Chang, Gleb Shtengel, ..., Wei Qiu, Harald F. Hess, Jennifer Lippincott-Schwartz

Correspondence

lippincottschwartzj@janelia.hhmi.org

In brief

Dynamic nano-anatomy of the mammalian early secretory pathway reveals that ER-to-Golgi trafficking is supported by an intertwined tubule receptacle, which is regulated by COPII and COPI and capable of extending microns along microtubules while still connected to ER by a narrow neck.

Weigel et al., 2021, Cell *184*, 2412–2429
April 29, 2021
https://doi.org/10.1016/j.cell.2021.03.035

CellPress

CellPress

Cell

Article

ER-to-Golgi protein delivery through an interwoven, tubular network extending from ER

Aubrey V. Weigel,[1,5] Chi-Lun Chang,[1,5] Gleb Shtengel,[1] C. Shan Xu,[1] David P. Hoffman,[2] Melanie Freeman,[1,3] Nirmala Iyer,[1] Jesse Aaron,[4] Satya Khuon,[4] John Bogovic,[1] Wei Qiu,[1] Harald F. Hess,[1] and Jennifer Lippincott-Schwartz[1,6,*]

[1]Janelia Research Campus, Howard Hughes Medical Institute, Ashburn, VA 20147, USA
[2]10X Genomics, Inc., Pleasanton, CA 94588, USA
[3]Advanced Bioimaging Center, Department of Molecular and Cell Biology, University of California, Berkeley, Berkeley, CA 94720, USA
[4]Advanced Imaging Center, Janelia Research Campus, Howard Hughes Medical Institute, Ashburn, VA 20147, USA
[5]These authors contributed equally
[6]Lead contact
*Correspondence: lippincottschwartzj@janelia.hhmi.org
https://doi.org/10.1016/j.cell.2021.03.035

SUMMARY

Cellular versatility depends on accurate trafficking of diverse proteins to their organellar destinations. For the secretory pathway (followed by approximately 30% of all proteins), the physical nature of the vessel conducting the first portage (endoplasmic reticulum [ER] to Golgi apparatus) is unclear. We provide a dynamic 3D view of early secretory compartments in mammalian cells with isotropic resolution and precise protein localization using whole-cell, focused ion beam scanning electron microscopy with cryo-structured illumination microscopy and live-cell synchronized cargo release approaches. Rather than vesicles alone, the ER spawns an elaborate, interwoven tubular network of contiguous lipid bilayers (ER exit site) for protein export. This receptacle is capable of extending microns along microtubules while still connected to the ER by a thin neck. COPII localizes to this neck region and dynamically regulates cargo entry from the ER, while COPI acts more distally, escorting the detached, accelerating tubular entity on its way to joining the Golgi apparatus through microtubule-directed movement.

INTRODUCTION

The secretory pathway is a foundational system used by all eukaryotic cells to distribute membrane and secretory proteins (Barlowe and Helenius, 2016). The first portage of this pathway—protein sorting at endoplasmic reticulum (ER) exit sites (ERESs) and transit to the Golgi apparatus—is orchestrated primarily by two evolutionarily conserved protein coat complexes, COPII and COPI, which each polymerize into flexible curved scaffolds to support membrane deformation and protein sorting (Aridor et al., 1995; Gomez-Navarro and Miller, 2016; Hanna et al., 2018; Rout and Field, 2017). COPII concentrates and sorts cargos into ERESs (Faini et al., 2013; Kuehn et al., 1998; Miller et al., 2003; Zanetti et al., 2013), which purportedly bud off vesicles that fuse with nearby vesicular-tubular clusters (Bannykh et al., 1996; Peotter et al., 2019; Zanetti et al., 2011; Zeuschner et al., 2006). COPI and its regulators are proposed to further differentiate the vesicular-tubular clusters into pre-Golgi intermediates enriched in p58 (Appenzeller et al., 1999; Schweizer et al., 1988) that subsequently sort and deliver proteins to the Golgi (Altan-Bonnet et al., 2004; Aridor et al., 1995; Béthune and Wieland, 2018; Stephens et al., 2000).

Various aspects of this trafficking model remain unclear. Conflicting data support the formation of the vesicular tubular clusters alternatively by homotypic fusion of COPII vesicles derived from the ER (Bannykh et al., 1996; Horstmann et al., 2002; Ladinsky et al., 1999) or by *en bloc* extrusion of the ER (Mironov et al., 2003) through tubules or tunnels (McCaughey et al., 2019; Raote and Malhotra, 2019) when cargo is synchronously released from ER. Another unknown is how COPI supports protein recycling to—and protein export from—the ER (Gomez-Navarro and Miller, 2016; Orci et al., 1997; Shima et al., 1999). Furthermore, the ability of pre-Golgi intermediates to bud vesicles targeted to the Golgi continues to be uncertain, as several live-cell imaging studies have shown that these compartments themselves move as transport carriers to the Golgi (Mironov et al., 2003; Presley et al., 1997; Scales et al., 1997; Stephens et al., 2000).

Many of these concerns remain unresolved in mammalian cells due to the absence of data on the 3D ultrastructural organization of ERESs and their derived transport intermediates in intact cells at isotropic, nanoscale resolution. Prior serial

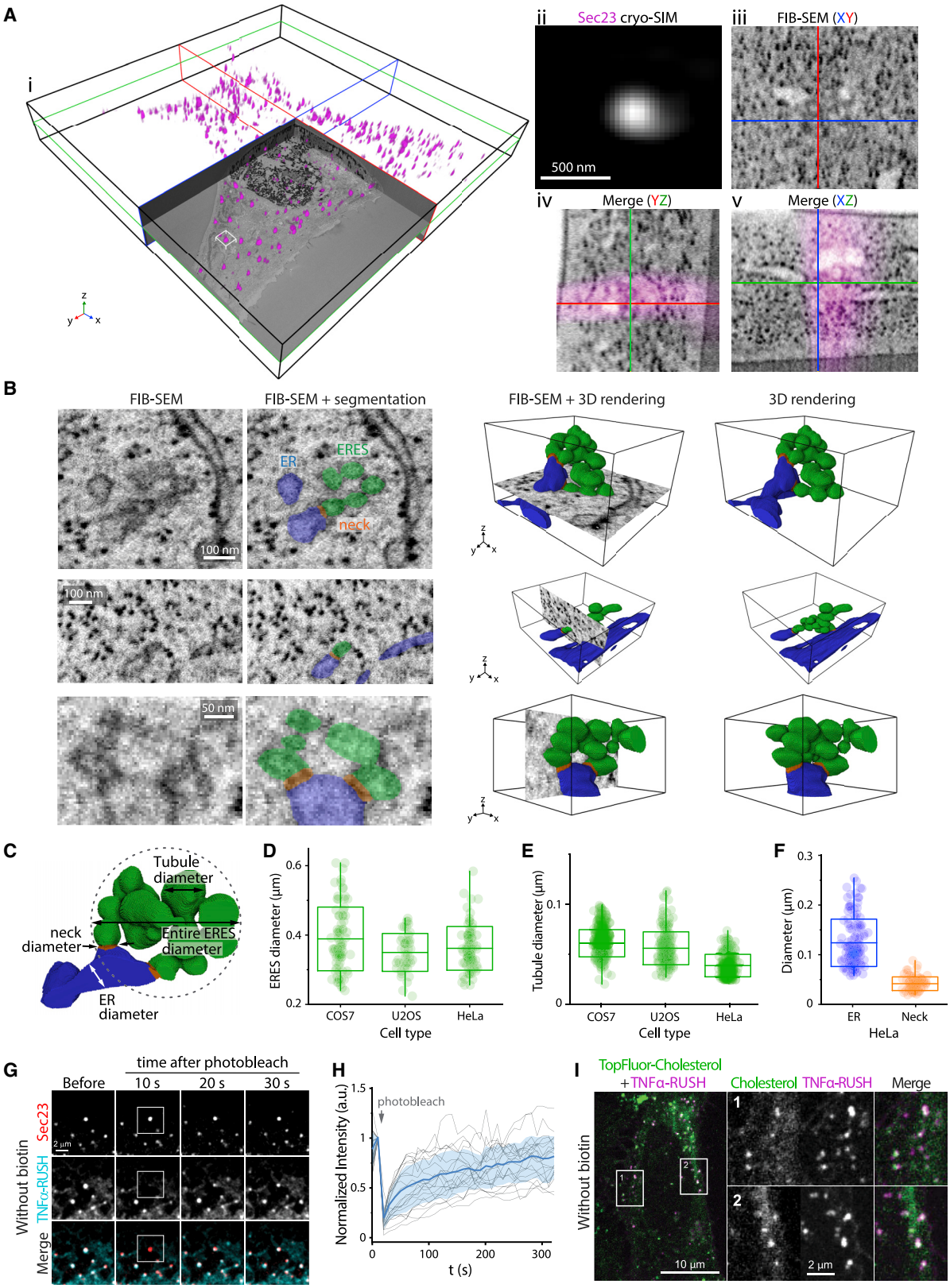

(legend on next page)

thin-section transmission electron microscopy (TEM) and tomographic approaches (Bannykh et al., 1996; Horstmann et al., 2002; Mironov et al., 2003; Zeuschner et al., 2006) have been limited by large section thickness, small sampling volume, and potential artifacts from chemical fixation. These deficiencies have made it difficult to fully reconstruct ERESs and transport intermediates and, thus, to understand how they function in secretory trafficking.

To overcome these difficulties, we applied whole-cell focused ion beam scanning electron microscopy (FIB-SEM) (Xu et al., 2017, 2020) combined with cryogenic-structured illumination microscopy (cryo-SIM) (Hoffman et al., 2020) to re-examine the ultrastructural features of ERESs and transport intermediates at isotropic, nanoscale resolution throughout an entire cell. To understand the functional significance of these compartments, we used Airyscan microscopy and fast confocal imaging, synchronized cargo release (Boncompain et al., 2012), and point localization analysis to dynamically define the localization of COPII, COPI, and cargos in relation to ERESs and transport intermediates.

Our results build on and transform previous thinking in this field (Bannykh et al., 1996; Gomez-Navarro and Miller, 2016; Mironov et al., 2003; Peotter et al., 2019; Shomron et al., 2019; Stephens et al., 2000). We show that ERESs consist of an intricate, tangled network of tubules connected by a neck to the ER. COPII and COPI facilitate separate steps within this receptacle, respectively acting to regulate secretory protein entrance into and departure from it. The overall size of the ERES increased in response to sudden cargo influx from ER, while its basic configuration remained unchanged. Extending off the ERESs alongside microtubules were tubular vessels with pearling shapes for protein transport to the Golgi. These vessels themselves advance toward the Golgi with no stable pre-Golgi compartments observed. Dynamic nano-anatomy reveals the ERES as an inter-organelle transport apparatus that actively modulates its shape and size while directing diverse cargo types to the Golgi.

RESULTS

Cryo-SIM/FIB-SEM characterization of ERESs

We applied cryo-SIM/FIB-SEM (Hoffman et al., 2020) to get a finer look at the 3D nano-anatomy of ERESs in mammalian cells. First, cells overexpressing fluorescent protein-tagged Sec23, a COPII coat protein known to localize at ERESs (Gomez-Navarro and Miller, 2016; Peotter et al., 2019), were high-pressure frozen to preserve their near-native states avoiding artifacts from chemical fixation. Next, cryo-SIM images were taken to obtain Sec23 features, followed by freeze-substitution, resin-embedding, and whole-cell FIB-SEM imaging. Cryo-SIM images of Sec23 (Figures 1Ai and 1Aii) were aligned to the FIB-SEM images (Figures 1Aiii–1Av) enabling objective identification and analysis of ERES ultrastructure with an isotropic resolution at 4–8 nm. We found that each ERES seen by FIB-SEM, identified by a single Sec23-positive punctum in cryo-SIM images, was composed of a cluster of vesicular-tubular membranes devoid of ribosomes near the ER (Figure 1Aiii), consistent with previous EM studies (Bannykh et al., 1996; Horstmann et al., 2002; Ladinsky et al., 1999).

Using this specific morphological identifier, hundreds of discrete ERESs in non-transfected cells were also identified to avoid potential artifacts of Sec23 overexpression (Figure 1B). Segmentation through serial FIB-SEM slices and 3D rendering provided a detailed isotropic view with 4-nm resolution of single ERESs. Each individual ERES comprised a highly intertwined tubule network, continuous with the ER by a constricted neck (Figure 1B, right panels, and 1C; Video S1). While some ERESs had only a single constricted neck attaching it to the ER, others had two or more. These features of ERESs were common in COS7, U2OS, and HeLa cells. The overall diameter of the tubule network was 350–390 nm (n = 207; 7 cells), while individual tubules in the tangled network had a diameter of 40–60 nm (n = 811; 7 cells) (Figures 1D and 1E). The neck region of the ERES was slightly constricted compared to the diameter of tubules in the tangled network, while nearby ER tubules were substantially wider (Figure 1F). Altogether, these results revealed that ERESs consist of an elaborate interwoven tubule network still attached to the ER. This distinct ERES anatomy would likely have been missed in earlier serial section TEM studies (Bannykh et al., 1996; Horstmann et al., 2002), as they used ~10 times less z resolution.

ERESs exchange contents with ER and can differentiate into a cholesterol-enriched environment

ERES continuity with the ER through a narrow neck raised the question of whether some membrane proteins could circulate between the ER and ERESs at steady state. We tested this in living cells using the retention using selective hooks (RUSH) system (Boncompain et al., 2012). This approach is based on reversible ER trapping of reporter cargos appended to streptavidin-binding peptide (SBP) via interaction with ER-localized streptavidin-fused "hook" proteins. Biotin addition competes the binding of streptavidin with SBP, leading to a synchronized

Figure 1. ERESs in intact mammalian cells revealed by cryo-SIM/FIB-SEM

(A) Identification of ERESs in FIB-SEM slices by cryo-SIM imaging of Halo-Sec23 (magenta) in HeLa cells. The whole-cell (i) and zoomed-in regions in white (ii–v) are shown with the Sec23 fluorescence alone (ii), FIB-SEM only (iii), and overlay of fluorescence and FIB-SEM in the YZ (iv) and XZ (v) views.

(B) Segmentation and 3D rendering of 3 peripheral ERESs from a HeLa cell without Sec23 overexpression.

(C) A diagram of an ERES from 3D rendering in (B) depicting different regions.

(D–F) Diameters of ERES (D), tubules (E), and connecting ER and neck (F) as described in (C). Raw data, means ± SD, and minimum-maximum range are indicated.

(G) Fluorescence recovery after photobleaching (FRAP) of Halo-TNF-α-RUSH in an ERES labeled by mEmerald-Sec23 from a HeLa cell monitored by confocal microscopy.

(H) FRAP analysis of TNF-α-RUSH as described in (G). Mean (blue line) from 21 regions (gray lines) in 3 experiments and SD (shaded blue) are indicated.

(I) Co-localization of TopFluor-Cholesterol and Halo-TNF-α-RUSH at ERESs in HeLa cells monitored by confocal microscopy.

See also Figure S1 and Table S1.

reporter cargo release into secretory compartments. We used a transmembrane secretory protein tumor necrosis factor α (TNF-α) as a RUSH reporter (TNF-α-RUSH) because, before biotin addition, TNF-α-RUSH displayed an ER distribution as well as being enriched at ERESs labeled by Sec23 or Sec31 (Figures 1G, S1A, and S1B) (Fourriere et al., 2016). Photobleaching of TNF-α-RUSH in a single ERES in cells with no biotin addition revealed that, after photobleaching, the intensity of TNF-α-RUSH fluorescence quickly returned within the ERES, reaching near-complete recovery in tens of seconds (Figures 1G, 1H, S1C, and S1D). This indicated that TNF-α-RUSH underwent rapid exchange between the ER and ERESs, consistent with the continuity of the ER and ERES membrane revealed by FIB-SEM.

Previous work has shown a requirement for cholesterol in ER-to-Golgi trafficking (Ridsdale et al., 2006). Supporting this requirement, we found that ERESs labeled with TNF-α-RUSH cargo had higher cholesterol levels compared to levels in the ER based on TopFluor-cholesterol imaging (Figure 1I). The cholesterol enrichment at ERESs could help sort certain cargo proteins at these sites, as cholesterol can partition lipids and proteins into subdomains within a continuous bilayer (Lingwood and Simons, 2010; Simunovic et al., 2019). It remains to be determined, however, whether ERESs are always cholesterol-enriched environments or only after they have accumulated specific secretory cargo types.

Enlargement of ERESs during RUSH cargo release

We next explored whether cargo accumulation changes the organization of ERESs. We examined ERESs by cryo-SIM/FIB-SEM during synchronized TNF-α-RUSH cargo release. First, the chronological events of TNF-α-RUSH release were characterized to determine the optimal time for cyro-fixation. Approximately 2–3 min after the addition of biotin, cells entered a synchronized release phase for 10–15 min, in which TNF-α-RUSH in the ER and ERESs underwent anterograde movement. As TNF-α-RUSH left ERESs via mobile, elongated transport intermediates (Figure S2A; Video S2), a sudden decrease in the intensity of TNF-α-RUSH at ERESs was observed (Figure S2B). After 12–18 min of biotin addition, TNF-α-RUSH could be seen accumulating in the Golgi (Figure S2C). Thus, we high-pressure-froze cells after 8 min of biotin addition to ensure that significant TNF-α-RUSH would still be at ERESs.

Cryo-SIM/FIB-SEM imaging revealed TNF-α-RUSH fluorescence localized to an intertwined tubule network connected by a neck to the ER (Figures 2A–2Av; Video S3), suggesting that these structures are the functional unit of protein exit from the ER. In addition, we saw no enrichment of vesicles near the TNF-α-RUSH-positive ERESs relative to random volumes in the cytoplasm (Figure S2D), suggesting that vesicles were not the primary transport vessels. Notably, segmentation and 3D rendering showed that the general organization of ERES during TNF-α-RUSH release remained similar to that in resting cells (Figures 2A and 2B). This suggested that sudden cargo accumulation did not fundamentally alter the organization of ERESs. However, the diameter of the entire ERES during TNF-α-RUSH release increased over 2-fold (Figures 2B and 2C). This coincided with enlargement of tubules within the network and connecting neck (Figures 2B and 2C). The diameters of the nearby ER, by contrast, remained unchanged (Figure 2C). Altogether, these results indicated that the size of the ERES and its associated tubules undergo dynamic regulation to accommodate a large quantity of membrane proteins into the secretory pathway, with no fundamental change in ERES organization.

Cargo entrance into ERESs and departure from ERESs are independent events

To better understand how such a distinctive organization of ERESs contributes to protein trafficking, we examined the kinetics of cargo entrance into and departure from ERESs using different RUSH cargos. We focused first on TNF-α-RUSH. Despite its pre-localization to ERESs, TNF-α-RUSH remained stationary at ERESs for 2–3 min after biotin addition without any anterograde movement and then moved robustly toward the Golgi, as indicated in the temporal projection map (Figure 2D; Video S2). This suggested that the ERES entrance and departure of TNF-α-RUSH are differentially regulated.

We next examined other RUSH cargos, including glycosylphosphatidylinositol (GPI)-anchored RUSH (GPI-RUSH), transferrin receptor (TfR)-RUSH (transmembrane cargo), and Gp135-RUSH (transmembrane cargo). Unlike TNF-α-RUSH, these RUSH cargos localized primarily in the ER before biotin addition (Figures 2E and S2E). After 2–3 min of biotin incubation, GPI-RUSH accumulated at ERESs, as reflected by an increase in intensity (Figures 2E and 2F). Each cargo type entered and accumulated at ERESs at distinct rates (Figure 2G). This suggested a specific gating mechanism for cargo entrance into ERESs, which may involve the differential affinity of cargo for COPII, cargo receptors, and/or the ERES's potentially cholesterol-rich membranes.

Once within an ERES, GPI-RUSH, TfR-RUSH, and Gp135-RUSH all displayed another stationary phase, ranging from 45 s to a few minutes, depending on cargo type (Figure 2H), before their movement toward the Golgi. This suggested that cargo departure is also differentially controlled, but through a different mechanism than that for cargo entry into ERESs. Altogether, these results suggest the ERES is a distinct early secretory compartment, with different gatekeeping mechanisms for regulating protein entry and departure.

COPII's role in cargo entry into ERESs

To explore COPII's potential gating function at ERESs, we focused on Sar1, a small GTPase responsible for assembling the COPII coat on membranes (Peotter et al., 2019). We used H89, a kinase inhibitor known to inhibit Sar1 recruitment to the ER (Aridor and Balch, 2000; Lee and Linstedt, 2000), to disrupt COPII assembly. Adding H89 to cells caused a rapid and sustained decrease in the intensity of Sec23 puncta, especially at the cell periphery, without noticeable changes in the ER and Golgi structure over the time period of imaging (Figures S3A and S3B). H89 treatment also led to a substantial reduction of TNF-α-RUSH intensity at ERESs (Figures 3A and 3B), suggesting that COPII assembly by Sar1-GTP is necessary for TNF-α-RUSH's entrance into ERESs. In addition, the presence of H89 prevented GPI-RUSH from entering and accumulating at ERESs after biotin addition (Figures S3C and S3D), supporting

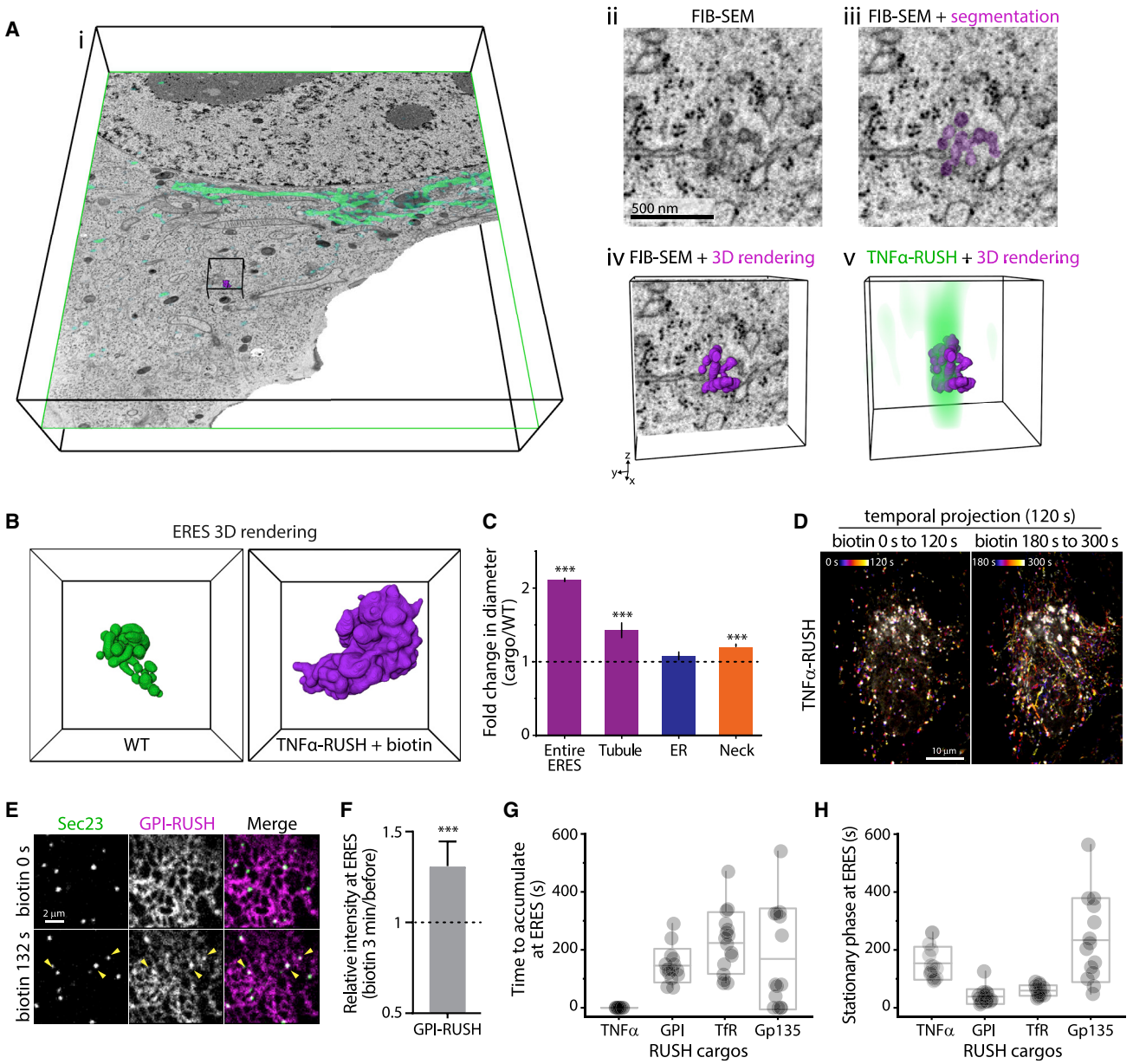

Figure 2. Dynamic regulation of ERESs during RUSH cargo release

(A) Segmentation and 3D rendering of an ERES from FIB-SEM slices in cells overexpressing mApple-TNF-α-RUSH cryo-frozen after 8 min of biotin addition. A quadrant of the whole cell (i) and zoomed in region boxed in black (ii–v) are indicated.

(B) 3D renderings of representative ERESs in control cell or in cell described in (A). Boxed regions are 1.2 μm × 1.2 μm × 0.9 μm.

(C) Relative changes in the diameter of ERESs, tubules, nearby ER, and neck in cells overexpressing RUSH cargos during biotin release. Mean ± SD are indicated.

(D) Temporal projections of a Halo-TNF-α-RUSH-overexpressing HeLa cell during biotin release monitored by confocal microscopy.

(E) Halo-GPI-RUSH enters ERESs labeled by mEmerald-Sec23 after biotin addition in a HeLa cell monitored by confocal microscopy. Yellow arrowheads indicate GPI-RUSH colocalized with Sec23.

(F) Relative intensity of GPI-RUSH at ERESs after 3 min of biotin addition. Mean ± SD are indicated (16 cells from 3 experiments).

(G) Time for RUSH cargo entry into ERESs after biotin addition. Raw data, mean ± SD, and minimum-maximum range are indicated (14–16 cells from 3 experiments).

(H) Retention time of RUSH cargo in ERESs before moving away from ERESs. Raw data, mean ± SD, and minimum-maximum range are shown (14–17 cells from 3 experiments).

See also Figure S2 and Table S1.

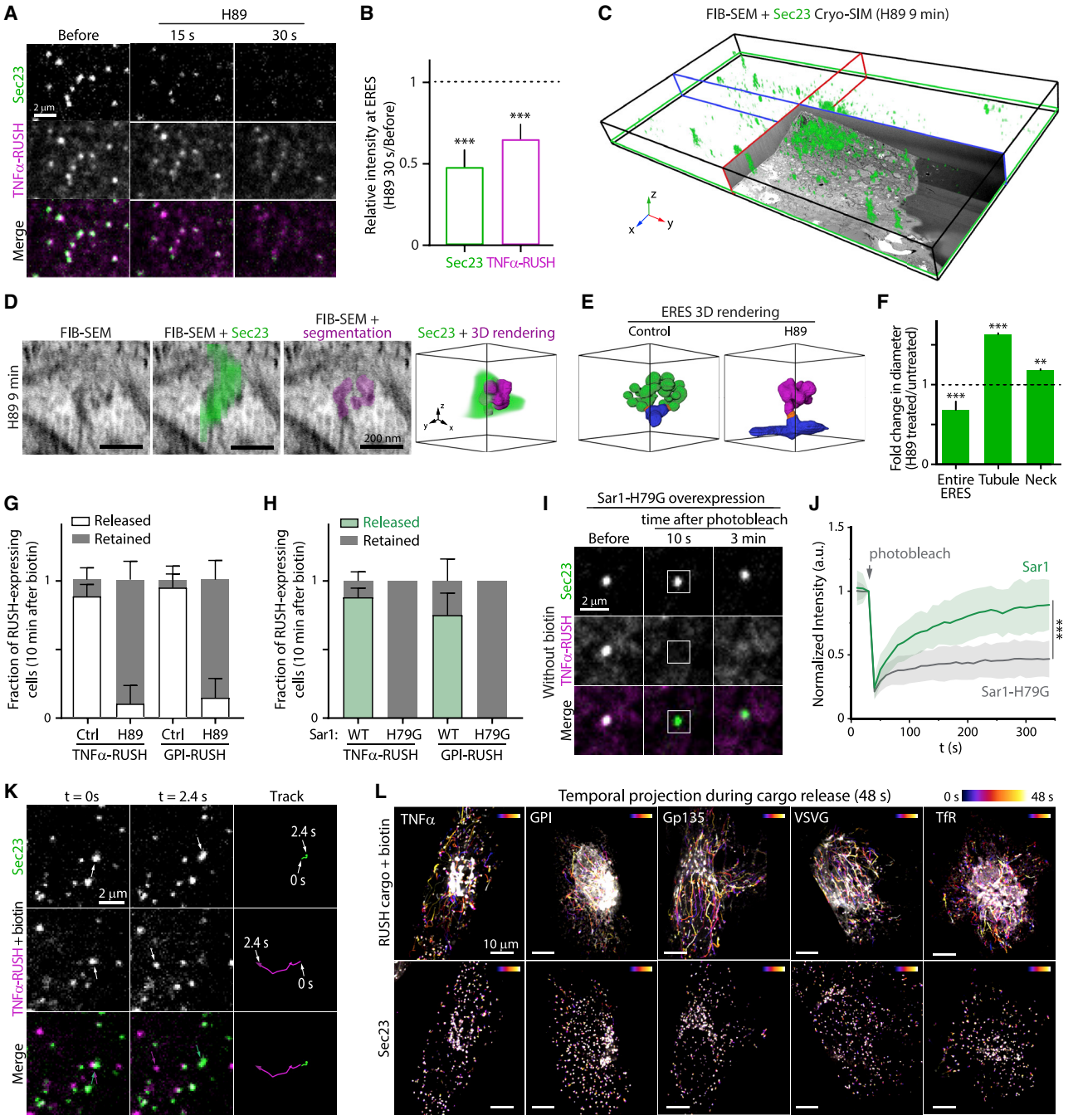

Figure 3. Dynamic assembly of COPII coats gates cargo into ERESs

(A and B) Decrease in intensity of mEmerald-Sec23 and Halo-TNF-α-RUSH at ERESs after 50 μM H89 treatment in HeLa cells monitored by confocal microscopy (A). Relative intensity (B) of Sec23 and TNF-α-RUSH are shown in mean ± SEM (17–18 cells from 2 experiments).

(C and D) Segmentation and 3D rendering of an ERES labeled by mEmerald-Sec23 from FIB-SEM slices in cells cryo-frozen 9 min after H89 treatment. The whole cell (C) and representative rendering of a zoomed-in region (D) are indicated.

(E) 3D rendering of representative ERESs in control cell or in cell described in (C). Boxed regions are 0.6 μm × 0.6 μm × 0.6 μm.

(F) Fold change of ERES, tubule, and connecting neck diameters after H89 treatment relative to non-treated cells. Mean ± SD are indicated.

(G) Fraction of cells with RUSH cargo retained in ER/ERESs or released into the secretory pathway for Golgi delivery based on confocal imaging of RUSH cargo after 10 min of biotin treatment in control or H89-treated HeLa cells. Mean ± SD are indicated (3–4 independent experiments).

(H) Fraction of cells with RUSH cargo retained in ER/ERESs or released into the secretory pathway in HeLa cells overexpressing Sar1 or Sar1-H79G after 10 min of biotin treatment. Mean ± SD are indicated (2–3 independent experiments).

(legend continued on next page)

the idea that cargo entry into ERESs requires COPII assembly (Peotter et al., 2019).

Because H89 treatment caused a substantial decrease, but not complete disappearance, of Sec23 puncta, we could identify Sec23 fluorescence in cryo-SIM to analyze their architecture by FIB-SEM under this condition (Figure 3C). Examining 200 Sec23-containing puncta in HeLa cells frozen at 9 min of H89 incubation, we found that 42% still had identifiable ERES architectures (Figures 3D and S3F). However, the overall size of these ERESs was significantly smaller with fewer tubule elements; additionally, the necks connecting these ERESs to ER were wider than that seen in control cells (Figures 3D–3F). Interestingly, the other 58% of Sec23 remnants under H89 treatment lacked any ERES architecture and instead displayed Sec23 within lysosome-like structures (Figures S3E and S3F). This suggested that ERESs are targeted to lysosomes when COPII assembly is perturbed by H89. We further found that RUSH cargos were retained in the ER without the presence of cargo movement to Golgi over 10 min of biotin release in nearly all H89-treated cells (Figures 3G and S3G). Together, these findings support a significant role for COPII activity in the formation and function of ERESs.

We used a GTP-locked Sar1 mutant, Sar1-H79G, to further examine the role of COPII in RUSH cargo release. Previous studies using fluorescence recovery after photobleaching (FRAP) have shown that Sec23 can no longer exchange on and off membranes in cells expressing Sar1-H79G, with the mutation effectively locking COPII on membranes (Forster et al., 2006; Ward et al., 2001). We found fewer yet larger Sec23 puncta in cells expressing Sar1-H79G (Figures S3H and S3I). Importantly, these structures no longer functioned as proper ERESs: GPI-RUSH cargo failed to efficiently enter these ERESs after biotin addition (Figure S3J), and no cell with Sar1-H79G overexpression was capable of releasing TNF-α- and GPI-RUSH into the secretory pathway for Golgi delivery (Figure 3H). While TNF-α-RUSH remained pre-localized to these sites in resting Sar1-H79G-expressing cells, the protein could no longer circulate between the ER and ERESs based on FRAP analysis (Figures 3I and 3J). These results suggest that the Sar1-dependent cycle of assembly/disassembly of COPII subunits is required for ER-ERES continuity and cargo sorting in ERESs.

We simultaneously imaged COPII and RUSH cargo during biotin release to examine their distribution relative to each other. Notably, both the inner Sec23 cargo adaptor subunit and outer Sec31 subunit of the COPII coat remained stationary, while transport intermediates carrying TNF-α-RUSH departed from ERESs (Figures 3K and S3K). Temporal projections of COPII and cargo at ERESs show that, after biotin addition, the RUSH cargos, including TNF-α, GPI, Gp135, vesicular stomatitis virus G protein (VSVG), and TfR, all exhibited directed motion from peripheral ERESs to the perinuclear Golgi region (Figures 3L and S3L). By contrast, Sec23 or Sec31 remained localized at ERESs and exhibited little movement over this period. This led us to conclude that COPII's primary role is to gate protein entry into ERESs, a function crucial to both the formation and maintenance of these structures.

Spatial arrangement of COPI at ERESs

Previous work has shown that COPI associates with ERESs and participates in protein departure from these sites (Scales et al., 1997; Stephens and Pepperkok, 2002). With these studies in mind, we investigated COPI's localization with respect to ERESs with Airyscan microscopy, providing a 1.4-fold increase in lateral resolution over conventional confocal imaging (Huff, 2015). Antibodies to the endogenous COPI subunit, βCOP, revealed COPI localized both to the Golgi and at peripheral ERESs labeled with Sec23 (Figure 4A). In the LdlF-CHO (Chinese hamster ovary) cell line stably expressing εCOP-YFP (εCOP-CHO) (Presley et al., 2002), εCOP-YFP also co-localized with peripheral ERESs labeled by Sec23 or Sec31 (Figures 4B and S4A), with approximately 70% of the peripheral ERESs decorated with COPI (Figure 4C). This percentage was slightly upregulated in cells incubated at 15°C for 2 h to buildup secretory cargo at ERESs (Saraste and Kuismanen, 1984) and during GPI-RUSH and TNF-α-RUSH release (Figures 4C, 4D, and S4B). This suggested that, when cargo accumulates in ERESs, more COPI associates with these sites.

After centroid fitting of COPII and COPI on ERESs, we found that they were separated by 140 ± 40 nm, with COPII closer to the ER and COPI further away based on ER labeling by Sec61 (Figures 4E and 4G). During RUSH cargo release, GPI-RUSH or TNF-α-RUSH appeared to occupy the space between Sec23 and βCOP at ERESs (Figures S4C and S4D) with similar ER-COPII-COPI orientation (Figures 4F and 4G). The results thus suggested that, while COPII localizes to ERES zones proximal to ER, COPI distributes to zones distal to ER, with secretory cargo enriched between the two.

We examined whether Sar1-dependent COPII activity is required for COPI's recruitment to ERESs using H89. We observed that colocalization of COPII and COPI was substantially abolished after H89 treatment in εCOP-CHO cells (Figure 4H), with both Sec23 and εCOP puncta diminishing and their localizations becoming dispersed within the cytoplasm. We further found that Sar1-H79G overexpression led to the dissociation of βCOP and εCOP from ERESs (Figures 4I, 4J, and S4E). The results thus suggest that COPI localization at ERESs occurs downstream of Sar1-GTPase activity, raising the possibility that COPII and COPI function sequentially at ERESs to support protein trafficking.

(I) FRAP of Halo-TNF-α-RUSH in a mEmerald-Sec23-labeled ERES from a HeLa cell co-transfected with Sar1-H79G-mApple monitored by confocal microscopy.
(J) FRAP analysis of TNF-α-RUSH as described in (I) and from the FRAP experiment performed in cells co-transfected with Sec23 and Sar1. Means (solid lines) from 26–28 regions from 3 experiments and SD (shadings) are shown.
(K) Halo-TNF-α-RUSH leaves an ERES labeled by mEmerald-Sec23 during biotin incubation monitored by continuous confocal imaging. Trajectories of individual Sec23 and TNF-α-RUSH puncta are indicated.
(L) Temporal projections of various RUSH cargos and mEmerald-Sec23 during biotin release monitored by continuous confocal imaging.
See also Figure S3 and Table S1.

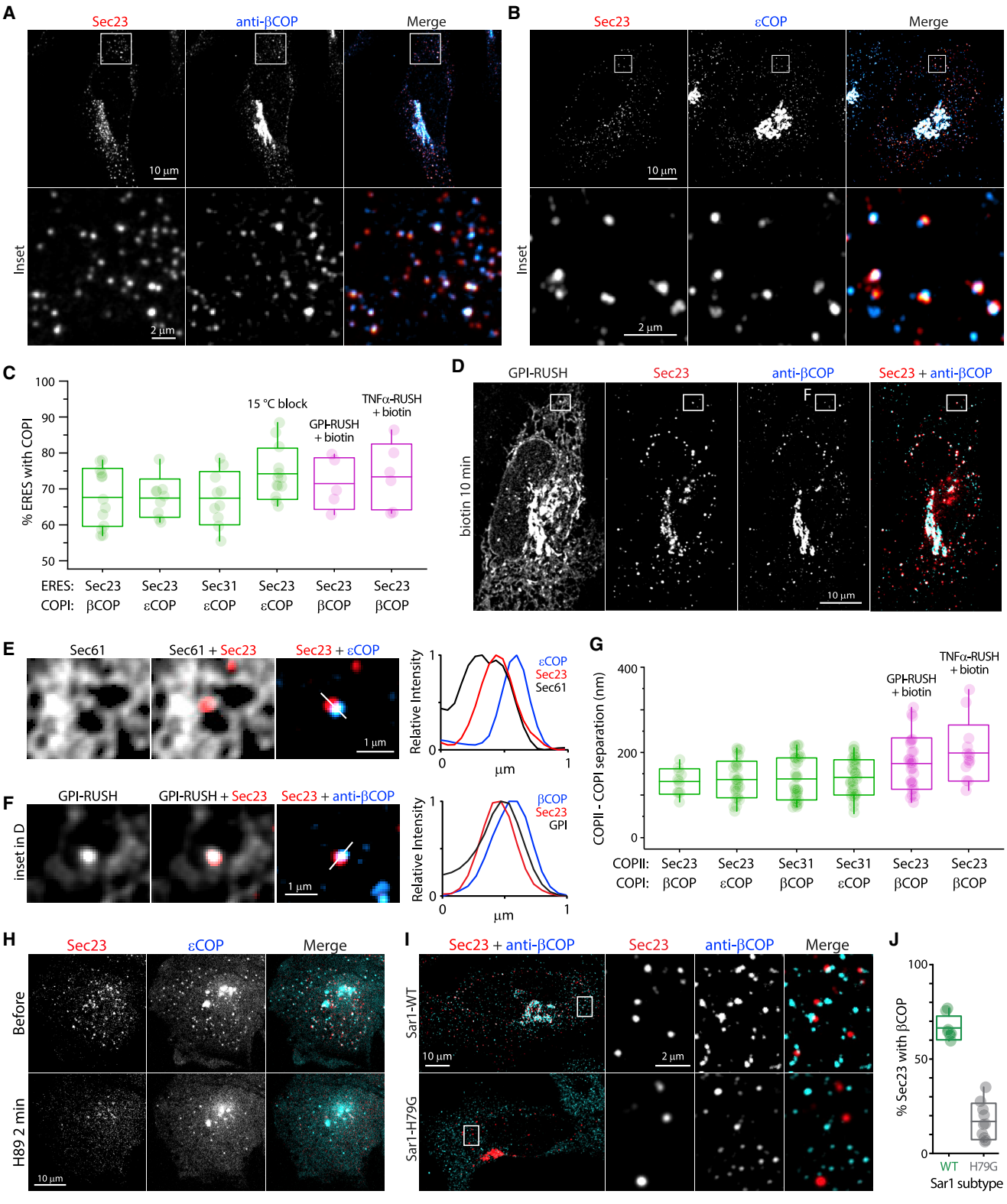

Figure 4. Spatial orientation of COPI and COPII at ERESs

(A) Colocalization of Halo-Sec23 and immunostained βCOP in fixed HeLa cells monitored by Airyscan microscopy. Inset shows white boxed area.

(B) Colocalization of Halo-Sec23 and εCOP-YFP in fixed εCOP-CHO cells monitored by Airyscan microscopy. Inset shows white boxed area.

(legend continued on next page)

COPI travels with transport intermediates containing RUSH cargos

Previous work has revealed that COPI accompanies temperature-sensitive VSVG-containing transport intermediates moving from the ER to Golgi (Shima et al., 1999; Stephens et al., 2000). To examine COPI's behavior during the departure of other cargos from ERESs, we monitored εCOP dynamics during synchronized release of different RUSH cargos. Examining TNF-α-RUSH first, we found that εCOP traveled with TNF-α-RUSH-containing transport intermediates as they moved away from ERESs upon biotin addition to cells (Figure 5A; Video S4). In whole-cell temporal projection traces, εCOP labeled RUSH cargo transport intermediates of TNF-α, GPI, Gp135, VSVG, and TfR, as they moved long distances, anterograde toward the Golgi (Figure 5B). Comparable εCOP trajectories could also be seen in εCOP-CHO cells without overexpression of RUSH cargo, suggesting that endogenous transport intermediates are labeled with εCOP (Figure S5A). Thus, COPI associates with diversely labeled anterograde transport intermediates from ERESs as they translocate toward the Golgi.

ERES function and ultrastructure when COPI is dissociated with BFA

To gain insight into the effect of COPI on ERESs and their derived transport intermediates, we examined ERESs in cells treated with BFA, a drug that inactivates Arf1 GTPase and thereby interferes with COPI membrane association and activities (Jackson and Casanova, 2000; Klausner et al., 1992). BFA treatment did not alter Sec23 localization at ERESs, despite causing: release of εCOP from these sites (Figure S5B); ER retention of both endogenous cargos (Klausner et al., 1992; Ward et al., 2001) and RUSH cargos after biotin incubation (Figure S5C); and the loss of ER-to-Golgi transport intermediates (Altan-Bonnet et al., 2004). Nonetheless, TNF-α-RUSH still circulated between the ER and ERESs in BFA-treated cells, as evidenced by its rapid recovery after photobleaching in ERESs (Figures 5C and 5D). ERESs thus persist during BFA treatment, but they are unable to generate transport intermediates targeted to the Golgi.

To analyze the ultrastructure of ERESs in a BFA-treated cell, we applied whole-cell cryo-SIM/FIB-SEM to mEmerald-Sec23-expressing cells frozen 6 min after BFA treatment. This time period was sufficient for BFA to dissemble COPI and early enough to avoid indirect structural changes of ERESs due to prolonged BFA treatment. Sec23-positive ERESs were identified throughout the 3D volume of the cell (Figure 5E; Video S5). Segmentation and volumetric rendering of these Sec23-positive ERESs revealed an interwoven tubule network connected to the ER (Figure 5F), similar to the general organization of ERESs in control cells. However, the overall diameter of the BFA-exposed ERESs was larger than in control cells, and the sizes of tubules in its tubule network were substantially enlarged while the neck was more constricted (Figures 5G and 5H).

Together, these results suggested that ERESs can still form and concentrate some cargos (i.e., TNF-α-RUSH) after BFA treatment, but these structures cannot sufficiently mature to bud off anterograde transport intermediates. Given that COPI normally localizes to ERESs and travels with transport intermediates to the Golgi, the results implicated COPI and other Arf1 effectors in the differentiation of transport intermediates derived from ERESs.

Ultrastructure of transport intermediates derived from ERESs

We next examined the ultrastructure of transport intermediates using cryo-SIM/FIB-SEM in TNF-α-RUSH-expressing cells frozen at 8 min of biotin release. Positive with TNF-α-RUSH fluorescence, the tubular transport intermediates extended many microns through the cytoplasm (Figure 6A). Remarkably, the tubules exhibited a pearled membrane shape, with repeated varicosities (Figures 6B and S6B; Video S6). TNF-α-RUSH fluorescence could be seen filling these varicosities (Figures 6B and S6C). The pearled tubule vessels were often immediately adjacent, or still connected, to an ERES (Figures 6Bc and 6Bd, green), and microtubules regularly ran parallel to them (Figure 6Bd, gray).

As can be seen from the showcased volume renderings in Figures 6C, S6B, and S6C, the TNF-α-RUSH-positive tubule transport intermediates displayed variations in length (2.4 ± 0.8 μm, n = 10) and shape, as well as in diameter (50 ± 20 nm; n = 89 pearls), periodicity (200 ± 10 nm; n = 89 pearls), and number of varicosities/pearls (9 ± 5; n = 10) (Figures 6D–6H; Video S6). Furthermore, these intermediates were not an artifact of RUSH-cargo overexpression, as they could also be found in non-transfected cells (Figure 6I), displaying the same characteristics as their RUSH-cargo bearing counterpart, including close proximity to an ERES, a pearled-membrane shape, and close

(C) Percentage of ERESs labeled by Sec23 or Sec31 colocalized with βCOP (in HeLa cells) or εCOP (in εCOP-CHO cells). 15°C block indicates incubating cells at 15°C for 2 h before fixation. RUSH cargos + biotin indicate RUSH cargo-expressing cells fixed after 10 min of biotin incubation. Raw data, mean ± SD, and minimum-maximum range are shown.
(D) Colocalization of Halo-Sec23, mApple-GPI-RUSH, and immunostained βCOP in HeLa cells fixed at 10 min after biotin addition monitored by Airyscan microscopy.
(E) Orientation of Halo-Sec23 and εCOP-YFP with respect to the ER labeled with mCherry-Sec61 in fixed εCOP-CHO cells monitored by Airyscan microscopy. Relative intensity profile (right) is indicated.
(F) Orientation of Halo-Sec23, mApple-GPI-RUSH and immunostained βCOP as described in (D). Relative intensity profile (right) is indicated.
(G) Offsets between COPII (Sec23 or Sec31) and COPI (βCOP or εCOP) in steady state or during RUSH cargo release. Raw data, mean ± SD, and minimum-maximum range are indicated.
(H) Disappearance of mCherry-Sec23 and εCOP-YFP puncta after H89 treatment in εCOP-CHO cells monitored by confocal microscopy.
(I) Distribution of Halo-Sec23 and immunostained βCOP in fixed HeLa cells overexpressing Sar1-mApple and Sar1-H79G-mApple monitored by Airyscan microscopy.
(J) Percentage of ERESs labeled by Sec23 colocalized with βCOP as described in (I). Raw data, mean ± SD, and minimum-maximum range are indicated.
See also Figure S4 and Table S1.

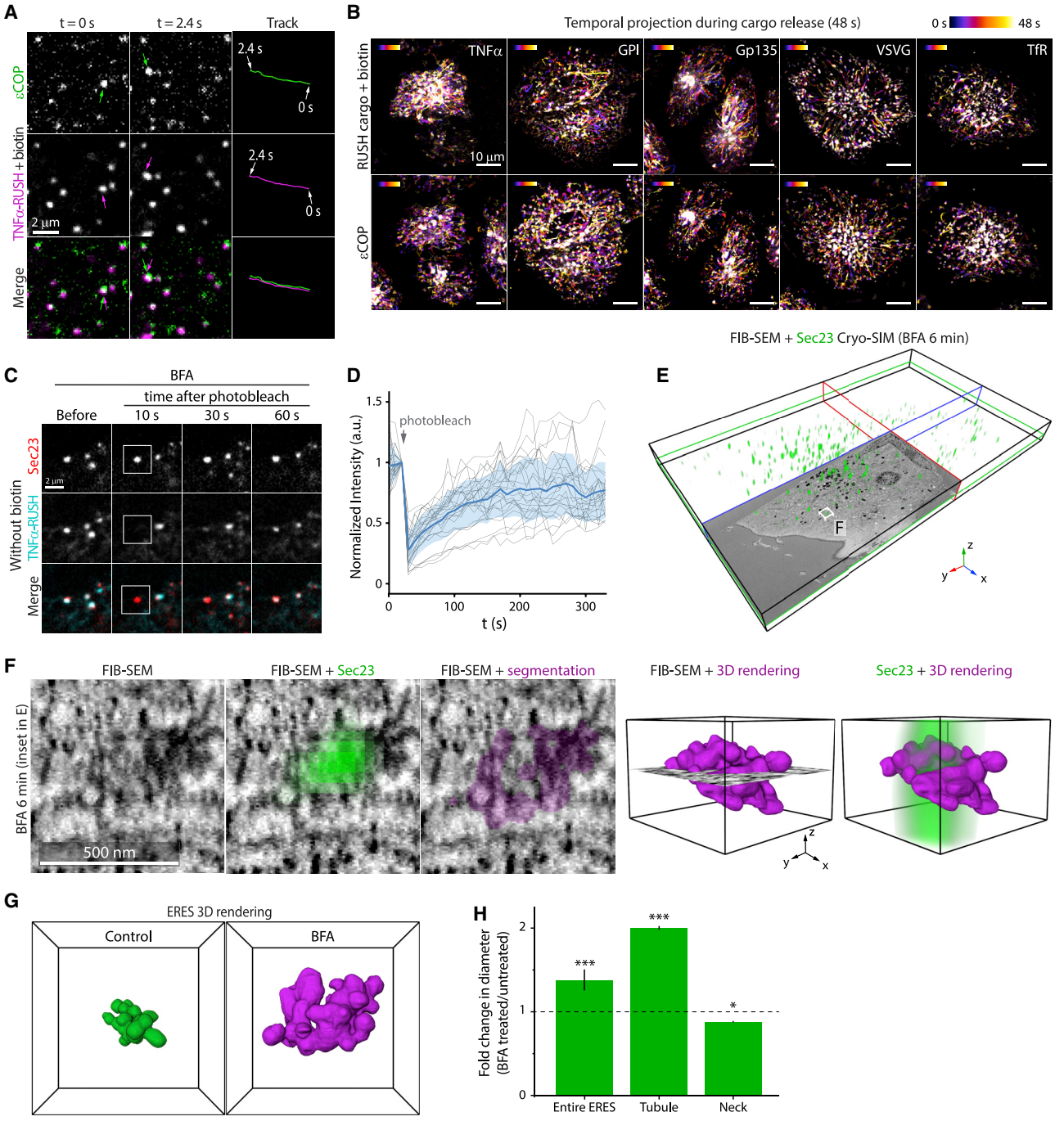

Figure 5. COPI travels coincidently with transport intermediates containing RUSH

(A) εCOP-YFP and Halo-TNF-α-RUSH leave ERESs in εCOP-CHO cells during biotin incubation monitored by continuous confocal imaging. Trajectories of individual TNF-α-RUSH and εCOP puncta are indicated.

(B) Temporal projections of RUSH cargos and εCOP in εCOP-CHO cells during biotin release monitored by continuous confocal imaging.

(C) FRAP of Halo-TNF-α-RUSH in a mEmerald-Sec23-labeled ERES from a HeLa cell during BFA treatment monitored by confocal microscopy.

(D) FRAP analysis of experiment described in (C). Mean (blue line) from 24 regions in 3 experiments (gray lines) and standard deviation (shaded blue) are indicated.

(E and F) Segmentation and 3D rendering of an ERES labeled with mEmerald-Sec23 from FIB-SEM slices in cells cryo-frozen 6 min after BFA treatment. The whole cell (E) and representative rendering of a zoomed-in region boxed in white (F) are indicated.

(G) 3D rendering of a representative ERES in control cells or in cells described in (E). Boxed regions are 1.2 μm × 1.2 μm × 0.9 μm.

(H) Fold change in ERES, tubule, and neck diameters after BFA treatment relative to non-treated cells. Mean ± SD are indicated.

See also Figure S5 and Table S1.

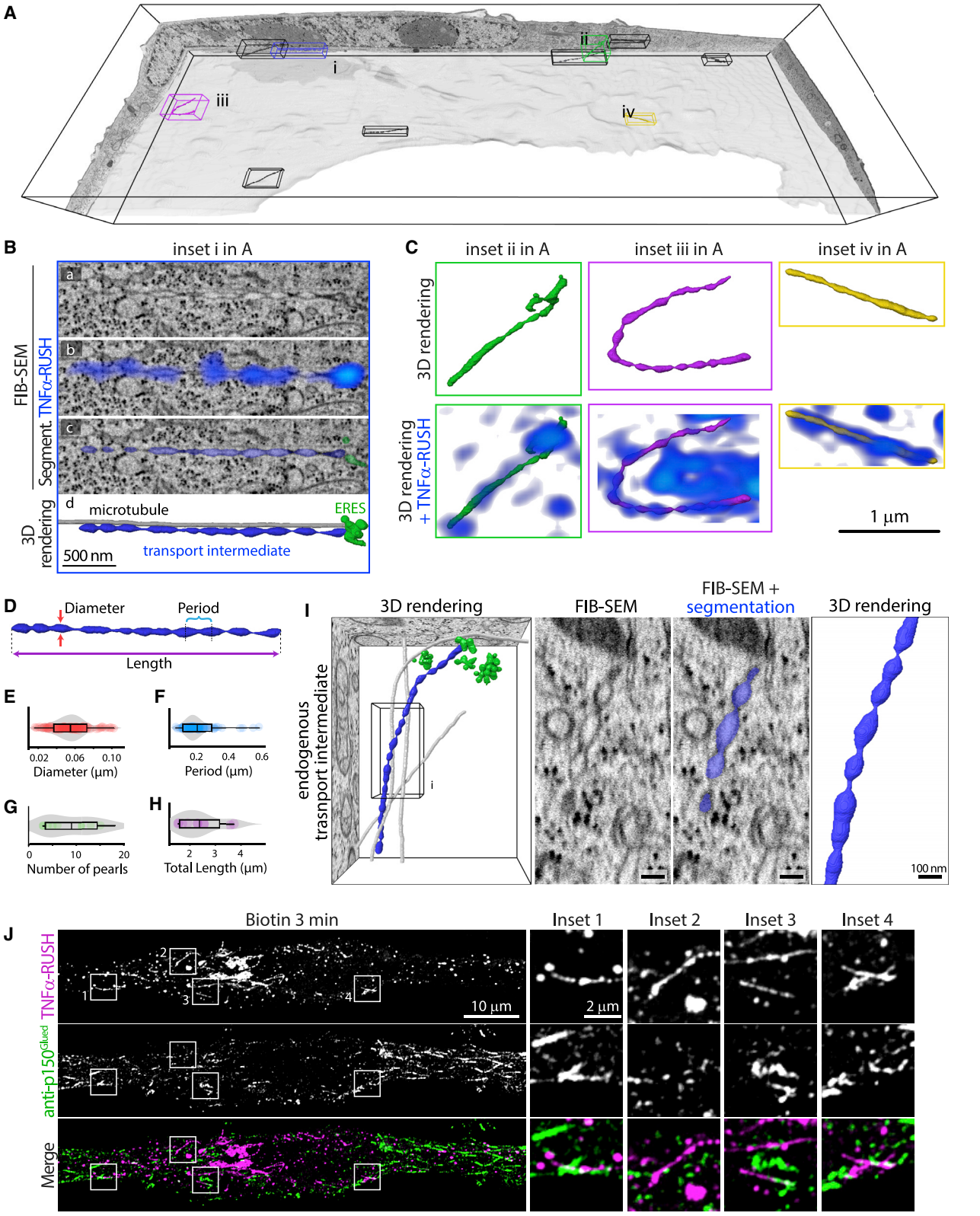

(legend on next page)

association with microtubules. These results suggested that the pearled transport intermediates may be a common, but not exclusive, vessel for delivery of secretory proteins to the Golgi.

The pearled membrane morphology of these transport intermediates is a characteristic of tubules under tension in model membrane systems (Bar-Ziv and Moses, 1994). This tension may be generated by microtubule-associated motors pulling on these transport intermediates. In fact, the dynactin motor complex has been shown to associate with ERESs through its interactions with COPII (Watson et al., 2005) and to mediate plus-to-minus end movement of transport intermediates containing temperature-sensitive VSVG along microtubules (Presley et al., 1997). Consistent with these previous studies, we found that endogenous p150^{Glued}, a subunit of the dynactin motor complex visualized by immunostaining, displayed recurrent association with elongated transport intermediates containing TNF-α-, GPI-, Gp135-, TfR-, or VSVG-RUSH cargos (Figures 6J and S6D). These observations support the idea that the pearled transport intermediate is under tension created by the dynactin motor complex.

ERES-derived transport intermediates are mobile structures with punctate COPI domains

Previous work has suggested the existence of an ER-Golgi intermediate compartment enriched in p58 that buds off vesicles for protein delivery to the Golgi (Peotter et al., 2019; Schweizer et al., 1988). To clarify the relationship between this purported intermediate compartment and the tubule transport carriers described earlier, we turned to live-cell imaging of RUSH-cargo, COPI, and p58 to obtain a dynamic picture of the system.

We found that fluorescent-protein-tagged p58 was concentrated at ERESs and in elongated tubular structures often linked to ERESs, coinciding with moderate ER and Golgi localization in resting cells (Figure S7A). In addition, an offset of 60 ± 30 nm (n = 25, 2 cells) between p58 and Sec23 in the same ERES was observed using Airyscan microscopy (Figures S7B and S7C). This offset is similar to the distance of secretory cargos to Sec23 (Figures S4D and S4E), suggesting that p58 localizes with these cargos in the mid-region of ERESs.

Significantly, time-lapse imaging revealed that p58-positive tubules were dynamic rather than stationary structures (Video S7). In addition, p150^{Glued} was often associated with p58-positive tubules (Figure S7D), reminiscent of transport intermediates for RUSH cargos. Indeed, p58 decorated and moved concurrently with transport intermediates containing RUSH cargos during biotin release (Figures 7A and 7B). Moreover, in the presence of TNF-α-RUSH, the transport intermediates differentiated into cholesterol-rich compartments (Figure 7C). These results suggested that, rather than being a stable compartment between ER and Golgi, p58-positive structures are motile transport intermediates, delivering cargo from ERESs to the Golgi. Consistent with this idea, overexpression of Sar1-H79G, which blocks the departure of RUSH cargo from the ER during biotin release, led to ER retention of p58 with no presence in mobile tubules (Figure 7D). This also coincided with ER retention of Golgi enzymes (Figures S7E and S7F).

We next examined the distribution of COPI coats on transport intermediates containing RUSH cargos and p58. Significantly, εCOP was localized to discrete foci on these transport intermediates (Figures 7E, 7F, and S7G). The number of εCOP microdomains appeared to be positively correlated with the length of the tubule transport vessel (Figure 7G). While εCOP mostly decorated the tips of these vessels (Figures 7E and S7G), longer transport intermediates often displayed additional εCOP puncta in their middle regions (Figure 7F). Similar distributions of COPI on transport intermediates were observed by βCOP immunostaining in cells fixed during RUSH cargo release (Figure S7H). This discrete distribution of COPI was not an artifact of RUSH cargo overexpression, as εCOP and βCOP foci were also observed on p58-positive tubes in non-RUSH-cargo-transfected cells (Figures 7H and S7H). Moreover, εCOP moved simultaneously with p58 tubules (Figures 7H and 7I), likely carrying endogenous protein cargos from the ER to Golgi. The βCOP microdomains on RUSH-cargo-containing or p58-positive transport intermediates did not colocalize with p150^{Glued} foci, although they were occasionally nearby (Figure S7H), suggesting that COPI components are not directly involved in coupling transport intermediates to microtubules.

DISCUSSION

A key issue in understanding the early secretory pathway and its remarkable adaptability to different cellular states has been how to bridge structural insights from *in vitro* reconstitution (Faini et al., 2013; Kuehn et al., 1998; Miller et al., 2003; Zanetti et al., 2013) with live-cell images capturing this pathway in operation (Bannykh et al., 1996; Presley et al., 1997; Scales et al., 1997). Our re-examination of the architecture and dynamics of the early secretory pathway using whole-cell FIB-SEM technology (Hoffman et al., 2020; Xu et al., 2017, 2020) in combination with

Figure 6. Transport intermediates often display pearled membrane morphology and associate with microtubules

(A) Segmentation and 3D rendering of transport intermediates carrying mApple-TNF-α-RUSH in a HeLa cell cryo-frozen after 8 min of biotin addition.

(B) FIB-SEM (a) with mApple-TNF-α-RUSH cryo-SIM (b), segmentation (c), and 3D volume rendering (d) are indicated for inset (i) in (A). Volume rendering indicates ERES (green), transport intermediate (blue), and adjacent microtubules (gray).

(C) Volume rendering (top panels) of inset (ii–iv) from (A) and their colocalization with mApple-TNF-α-RUSH cryo-SIM (bottom panels).

(D) A diagram of a transport intermediate from 3D rendering in (B) depicting pearl diameters, periods, and total length.

(E–H) Quantification of transport intermediates diameters (E), periods (F), number of pearls (G), and total length (H), as described in (D). Raw data distribution, mean ± SD, and minimum-maximum range are shown.

(I) Segmentation and 3D rendering of a transport intermediate in a non-transfected HeLa cell. Volume rendering indicates ERES (green), transport intermediate (blue), and adjacent microtubules (gray).

(J) Colocalization of Halo-TNF-α-RUSH transport intermediates and a dynein motor protein component p150^{Glued} (immunostained) in a fixed HeLa cell monitored by Airyscan microscopy.

See also Figure S6 and Table S1.

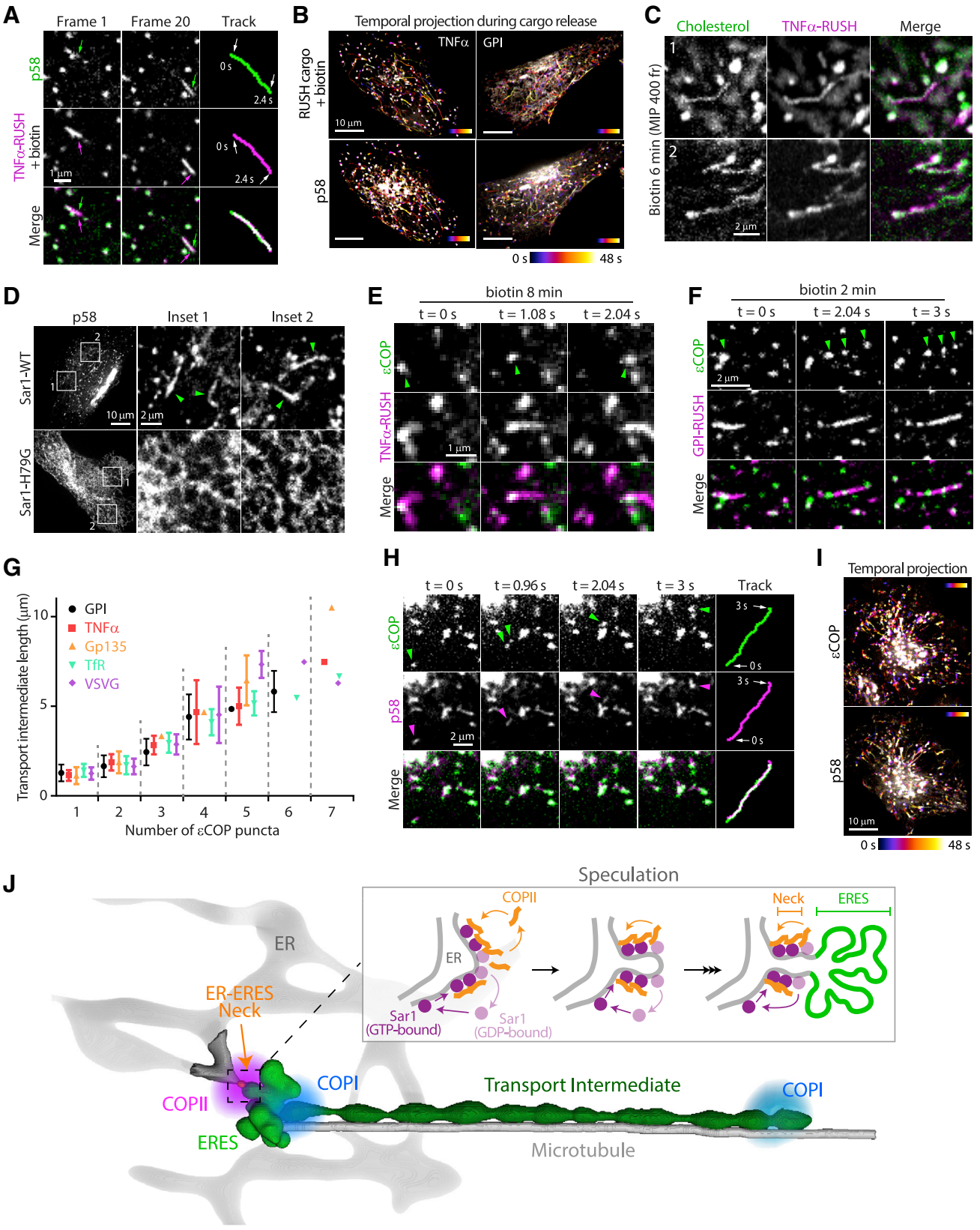

(legend on next page)

multi-modality light microscopy enhances this understanding and, at the same time, significantly transforms it. We showed that, rather than being composed of vesicle-like clusters budded out from nearby ER membranes, as previously suggested (Aridor, 2018; Bannykh et al., 1996; Horstmann et al., 2002), ERESs are intertwined tubules still in continuity with the ER by a narrow neck (Figure 7J). This entangled, tubular structure has a diameter of ~350–390 nm, with COPII distributed closer to the neck and COPI nearer to its rims. When secretory cargo was released into ERESs as a bolus, tubules within the meshwork increased in diameter, and the overall ERES size enlarged. Transport intermediates originating at ERESs were associated with microtubules and appeared as long pearled tubules carrying COPI, but not COPII, on their surface (Figure 7J). The earlier serial section TEM approaches, with 10 times less z resolution and a small sampling volume, may have mis-interpreted intertwined tubules as vesicles and missed elongated tubule transport intermediates extending many microns through the cytoplasm.

We envision that, rather than budding off small COPII vesicles, as occurs in *in vitro* systems, the flexible COPII coat remains associated at the neck region of ERESs through a continuous assembly/disassembly cycle controlled by Sar1-GTPase (Long et al., 2010) (see speculative model in Figure 7J). This cycle would create high membrane curvature for stabilization of a narrow neck (Hanna et al., 2016; Hariri et al., 2014; Loftus et al., 2012). Steric hindrance by large proteins such as Tango1L (Saito et al., 2009), which assembles into ring structures at the base of budding ER membranes (Raote et al., 2018), could further stabilize the neck by preventing scission (Raote and Malhotra, 2021). Membrane proteins recruited by COPII could then move into and through this neck, producing a bulging, budding domain that develops into an entangled tubule network (Bacia et al., 2011). Supporting this, when COPII was dissociated from ERESs under H89 treatment, cargo proteins at ERESs quickly returned to ER. Airyscan localization analysis further revealed COPII to be more closely positioned to the ER, shown also in previous EM studies (Bannykh et al., 1996; Mironov et al., 2003).

How could newly synthesized cargo proteins sort and concentrate at ERESs if these structures are still connected to the ER by a neck? An important implication of ERESs being a cholesterol-rich environment is that it would create a membrane domain that can dynamically retain membrane proteins and lipids by a partitioning mechanism (Baumgart et al., 2007; Sengupta et al., 2019; Simons and Vaz, 2004), thereby helping to sort and concentrate cargos into ERESs. Whether cargo receptors, such as Surf4 (Mitrovic et al., 2008), contribute to cargo entrance and enrichment of cholesterol at ERESs requires further investigation. This may provide insights into how this continuous membrane system can be tailored for different cargos.

Our data, in agreement with others, showed that COPII remains on ERESs and does not move forward with Golgi-bound transport intermediates (Shomron et al., 2019; Stephens et al., 2000; Westrate et al., 2020), suggesting that COPII does not directly control cargo exit from ERESs. We envision this role to be played by COPI and other Arf1 effectors (García et al., 2011; Monetta et al., 2007; Niu et al., 2005; Pind et al., 1994). This could be achieved if COPI and other Arf1 effectors on ERESs serve to differentiate these sites through recruitment, retention, and recycling of various proteins (Altan-Bonnet et al., 2004; Aridor et al., 1995; Lee et al., 2004; Monetta et al., 2007; Orci et al., 1997; Presley et al., 2002; Shima et al., 1999). This activity would likely take place in the middle to peripheral zones of ERESs, where COPI, cargos, and p58 were all localized. The COPI puncta observed at the tips or mid-sections of the tubule carriers could represent domains for further protein cargo sorting or retrieval back to the ER.

In summary, the ultrastructural and dynamic details of ERESs that we observed supports a model for protein trafficking fidelity at ERESs achieved by sequential actions of COPII and COPI within a continuous membrane system. This model of ERES functioning allows secretory transport to be tailored for cargos with various sizes, different cargo loads, or nonselective bulk flow of luminal proteins. This framework may also explain how large cargo such as procollagen exits the ER, as supported by a recent study demonstrating that procollagen travels coincidently with p58 (Omari et al., 2020). The different rates of cargo entry into and exit from ERESs that we observed could be explained by differential affinity of cargo for COPII or cargo receptors and/or the attraction of cargo to the ERES's apparent cholesterol-rich, lipid environment. Previous work has shown

Figure 7. Transport intermediates are mobile pre-Golgi compartments

(A) GFP-p58 colocalized with transport intermediates containing Halo-TNF-α-RUSH during biotin incubation monitored by continuous confocal imaging. Trajectories of individual GFP-p58 and TN-Fα-RUSH tubes are indicated.

(B) Temporal projections over 48 s of RUSH cargos and GFP-p58 during biotin release monitored by continuous confocal imaging.

(C) Co-localization of TopFluor-cholesterol and Halo-TNF-α-RUSH transport intermediates in HeLa cells during biotin release monitored by confocal microscopy. Maximal intensity projections (MIPs) of 400 continuously imaged frames (fr) are indicated.

(D) Distribution of GFP-p58 in HeLa cells co-transfected with Sar1-mApple or Sar1-H79G-mApple monitored by confocal microscopy. Green arrowheads indicate mobile p58 tubes.

(E and F) Punctate distribution of εCOP-YFP (green arrowheads) on transport intermediates containing Halo-TNF-α-RUSH (E) and GPI-RUSH (F) during biotin release in εCOP-CHO cells.

(G) Transport intermediate length categorized by associated εCOP puncta in εCOP-CHO cells overexpressing RUSH cargos during biotin incubation. Mean ± SD are indicated.

(H) εCOP-YFP foci (green arrowheads) travel on a mobile Halo-p58 tubes (magenta arrow heads) in εCOP-CHO cells. Trajectory of individual εCOP and p58 shown.

(I) Temporal projections over 48 s of Halo-p58 and εCOP-YFP in εCOP-CHO cells monitored by continuous confocal imaging.

(J) Model summarizing our results revealing the distributions of COPII (pink) and COPI (blue) in an ERES (green) and its associated transport carrier (dark green). Inset provides a speculative view for Sar1-dependent COPII activity at the ER-ERES neck, which gates cargo entry into the protruding tubule elements of the ERES.

See also Figure S7 and Table S1.

that spatial segregation of proteins and lipids can occur in continuous bilayer systems from membrane curvature and lipid partitioning effects (King et al., 2020; Sengupta et al., 2019; Seo et al., 2017; Simunovic et al., 2019; Toulmay and Prinz, 2013; Zhu et al., 2012). Our data fit well with this process taking place at ERESs in mammalian cells. Whether a similar mechanism is used in yeast and plants, where COPII vesicles seem to be the primary vessels for protein trafficking (Donohoe et al., 2013; Gomez-Navarro et al., 2020), remains to be explored. If correct, our model would help explain the adaptability of secretory trafficking in healthy and diseased states, including the ERESs' dynamic control over multiple functions involved in the quality control of protein sorting (Ge et al., 2017; Graef et al., 2013; Omari et al., 2018; Satpute-Krishnan et al., 2014; Subramanian et al., 2019; van Leeuwen et al., 2018).

Limitations of the study

The proposed model is primarily based on our FIB-SEM and light microscopy data in model cell lines with overexpressing coat proteins and/or cargos, so additional work using secretory components at their endogenous and physiological levels will be needed to verify its conclusions and predictions. Other work needed to extend the conclusions of this study includes examining ERESs and transport intermediates by FIB-SEM technology within cells in tissues rather than in dishes. This will allow assessment of the model in diverse cell types that exhibit large differences in cargo identities, abundances, and sizes. Other open questions that this study has not fully addressed and that remain to be investigated are: the mechanism(s) behind the formation of ERESs and transport intermediates; how receptor-cargo complexes shuttle through COPII and COPI gates to depart from ERESs; and how ERESs adapt their size to accommodate large cargos, such as collagens and lipoproteins.

STAR★METHODS

Detailed methods are provided in the online version of this paper and include the following:

- KEY RESOURCES TABLE
- RESOURCE AVAILABILITY
  - Lead contact
  - Materials availability
  - Data and code availability
- EXPERIMENTAL MODEL AND SUBJECT DETAILS
  - Cell culture
  - DNA plasmids
- METHOD DETAILS
  - Fluorescence microscopy imaging
  - Cell fixation and immunostaining
  - TopFluor-cholesterol labeling
  - Cryo-SIM/FIB-SEM and analysis
  - jrc_hela-21
  - jrc_hela-22
  - jrc_hela-bfa
  - jrc_hela-h89-1
  - jrc_hela-h89-2
  - jrc_hela-1
  - jrc_hela-2
  - jrc_hela-3
- QUANTIFICATION AND STATISTICAL ANALYSIS
  - Image analysis
  - Statistical analysis

SUPPLEMENTAL INFORMATION

Supplemental information can be found online at https://doi.org/10.1016/j.cell.2021.03.035.

ACKNOWLEDGMENTS

We thank Dr. Luke Lavis at the Janelia Research Campus, Howard Hughes Medical Institute, for providing JF Halo ligands; Dr. Gaelle Boncompain from Institute Curie, Paris, France and Dr. Prabuddha Sengupta at the Janelia Research Campus for generating constructs; Dr. H. Amalia Pasolli at Rockefeller University for technical assistance for FIB-SEM experiments; Dr. Brett Mensh and Dr. Carolyn Ott at the Janelia Research Campus for editing the manuscript; and Victoria Custard and Kerry Sobieski for administrative assistance. Many of the datasets used in this research were derived from a HeLa cell line derived from the tumor cells of Henrietta Lacks. The Advanced Imaging Center at Janelia Research Campus is a facility jointly supported by the Gordon and Betty Moore Foundation and the Howard Hughes Medical Institute. This work was supported by the Howard Hughes Medical Institute, Janelia Research Campus.

AUTHOR CONTRIBUTIONS

A.V.W., C.-L.C., and J.L.-S. conceived and designed the study. A.V.W. and C.-L.C. performed all experiments except cryo-SIM/FIB-SEM. A.V.W. and C.-L.C. prepared samples for live-cell imaging. A.V. W., C.-L.C., M.F., S.K., and N.I. prepared samples for cryo-CLEM. G.S., J.A., and D.P.H. performed cryo-SIM. C.S.X., G.S., and W.Q. acquired FIB-SEM data. H.F.H. supervised the FIB-SEM data acquisition. J.B. and A.V.W. registered the cryo-CLEM data. A.V.W. and C.-L.C. analyzed the data. A.V.W., C.-L.C., and J.L.-S. wrote the manuscript, with the input from all coauthors. J.L.-S. supervised the project.

DECLARATION OF INTERESTS

C.S.X. and H.F.H. have a U.S. patent 10,600,615 of the enhanced FIB-SEM system used in this work.

Received: May 4, 2020
Revised: December 23, 2020
Accepted: March 16, 2021
Published: April 13, 2021

REFERENCES

Altan-Bonnet, N., Sougrat, R., and Lippincott-Schwartz, J. (2004). Molecular basis for Golgi maintenance and biogenesis. Curr. Opin. Cell Biol. *16*, 364–372.

Appenzeller, C., Andersson, H., Kappeler, F., and Hauri, H.P. (1999). The lectin ERGIC-53 is a cargo transport receptor for glycoproteins. Nat. Cell Biol. *1*, 330–334.

Aridor, M. (2018). COPII gets in shape: Lessons derived from morphological aspects of early secretion. Traffic *19*, 823–839.

Aridor, M., and Balch, W.E. (2000). Kinase signaling initiates coat complex II (COPII) recruitment and export from the mammalian endoplasmic reticulum. J. Biol. Chem. *275*, 35673–35676.

Aridor, M., Bannykh, S.I., Rowe, T., and Balch, W.E. (1995). Sequential coupling between COPII and COPI vesicle coats in endoplasmic reticulum to Golgi transport. J. Cell Biol. *131*, 875–893.

Bacia, K., Futai, E., Prinz, S., Meister, A., Daum, S., Glatte, D., Briggs, J.A., and Schekman, R. (2011). Multibudded tubules formed by COPII on artificial liposomes. Sci. Rep. *1*, 17.

Bannykh, S.I., Rowe, T., and Balch, W.E. (1996). The organization of endoplasmic reticulum export complexes. J. Cell Biol. *135*, 19–35.

Bar-Ziv, R., and Moses, E. (1994). Instability and "pearling" states produced in tubular membranes by competition of curvature and tension. Phys. Rev. Lett. *73*, 1392–1395.

Barlowe, C., and Helenius, A. (2016). Cargo Capture and Bulk Flow in the Early Secretory Pathway. Annu. Rev. Cell Dev. Biol. *32*, 197–222.

Baumgart, T., Hammond, A.T., Sengupta, P., Hess, S.T., Holowka, D.A., Baird, B.A., and Webb, W.W. (2007). Large-scale fluid/fluid phase separation of proteins and lipids in giant plasma membrane vesicles. Proc. Natl. Acad. Sci. USA *104*, 3165–3170.

Béthune, J., and Wieland, F.T. (2018). Assembly of COPI and COPII Vesicular Coat Proteins on Membranes. Annu. Rev. Biophys. *47*, 63–83.

Bogovic, J.A., Hanslovsky, P., Wong, A., and Saalfeld, S. (2016). Robust Registration of Calcium Images by Learned Contrast Synthesis. In Proceedings of the 2016 IEEE 13th International Symposium on Biomedical Imaging (IEEE), pp. 1123–1126, https://ieeexplore.ieee.org/document/7493463.

Boncompain, G., Divoux, S., Gareil, N., de Forges, H., Lescure, A., Latreche, L., Mercanti, V., Jollivet, F., Raposo, G., and Perez, F. (2012). Synchronization of secretory protein traffic in populations of cells. Nat. Methods *9*, 493–498.

Cole, N.B., Smith, C.L., Sciaky, N., Terasaki, M., Edidin, M., and Lippincott-Schwartz, J. (1996). Diffusional mobility of Golgi proteins in membranes of living cells. Science *273*, 797–801.

Donohoe, B.S., Kang, B.H., Gerl, M.J., Gergely, Z.R., McMichael, C.M., Bednarek, S.Y., and Staehelin, L.A. (2013). Cis-Golgi cisternal assembly and biosynthetic activation occur sequentially in plants and algae. Traffic *14*, 551–567.

Faini, M., Beck, R., Wieland, F.T., and Briggs, J.A. (2013). Vesicle coats: structure, function, and general principles of assembly. Trends Cell Biol. *23*, 279–288.

Forster, R., Weiss, M., Zimmermann, T., Reynaud, E.G., Verissimo, F., Stephens, D.J., and Pepperkok, R. (2006). Secretory cargo regulates the turnover of COPII subunits at single ER exit sites. Curr. Biol. *16*, 173–179.

Fourriere, L., Divoux, S., Roceri, M., Perez, F., and Boncompain, G. (2016). Microtubule-independent secretion requires functional maturation of Golgi elements. J. Cell Sci. *129*, 3238–3250.

Fourriere, L., Kasri, A., Gareil, N., Bardin, S., Bousquet, H., Pereira, D., Perez, F., Goud, B., Boncompain, G., and Miserey-Lenkei, S. (2019). RAB6 and microtubules restrict protein secretion to focal adhesions. J. Cell Biol. *218*, 2215–2231.

García, I.A., Martinez, H.E., and Alvarez, C. (2011). Rab1b regulates COPI and COPII dynamics in mammalian cells. Cell. Logist. *1*, 159–163.

Ge, L., Zhang, M., Kenny, S.J., Liu, D., Maeda, M., Saito, K., Mathur, A., Xu, K., and Schekman, R. (2017). Remodeling of ER-exit sites initiates a membrane supply pathway for autophagosome biogenesis. EMBO Rep. *18*, 1586–1603.

Gomez-Navarro, N., and Miller, E. (2016). Protein sorting at the ER-Golgi interface. J. Cell Biol. *215*, 769–778.

Gomez-Navarro, N., Melero, A., Li, X.H., Boulanger, J., Kukulski, W., and Miller, E.A. (2020). Cargo crowding contributes to sorting stringency in COPII vesicles. J. Cell Biol. *219*, e201806038.

Graef, M., Friedman, J.R., Graham, C., Babu, M., and Nunnari, J. (2013). ER exit sites are physical and functional core autophagosome biogenesis components. Mol. Biol. Cell *24*, 2918–2931.

Gustafsson, M.G., Shao, L., Carlton, P.M., Wang, C.J., Golubovskaya, I.N., Cande, W.Z., Agard, D.A., and Sedat, J.W. (2008). Three-dimensional resolution doubling in wide-field fluorescence microscopy by structured illumination. Biophys. J. *94*, 4957–4970.

Hanna, M.G., 4th, Mela, I., Wang, L., Henderson, R.M., Chapman, E.R., Edwardson, J.M., and Audhya, A. (2016). Sar1 GTPase Activity Is Regulated by Membrane Curvature. J. Biol. Chem. *291*, 1014–1027.

Hanna, M.G., Peotter, J.L., Frankel, E.B., and Audhya, A. (2018). Membrane Transport at an Organelle Interface in the Early Secretory Pathway: Take Your Coat Off and Stay a While: Evolution of the metazoan early secretory pathway. BioEssays *40*, e1800004.

Hariri, H., Bhattacharya, N., Johnson, K., Noble, A.J., and Stagg, S.M. (2014). Insights into the mechanisms of membrane curvature and vesicle scission by the small GTPase Sar1 in the early secretory pathway. J. Mol. Biol. *426*, 3811–3826.

Hoffman, D.P., Shtengel, G., Xu, C.S., Campbell, K.R., Freeman, M., Wang, L., Milkie, D.E., Pasolli, H.A., Iyer, N., Bogovic, J.A., et al. (2020). Correlative three-dimensional super-resolution and block-face electron microscopy of whole vitreously frozen cells. Science *367*, eaaz5357.

Horstmann, H., Ng, C.P., Tang, B.L., and Hong, W. (2002). Ultrastructural characterization of endoplasmic reticulum–Golgi transport containers (EGTC). J. Cell Sci. *115*, 4263–4273.

Huff, J. (2015). The Airyscan detector from ZEISS: confocal imaging with improved signal-to-noise ratio and super-resolution. Nat. Methods *12*, i–ii.

Jackson, C.L., and Casanova, J.E. (2000). Turning on ARF: the Sec7 family of guanine-nucleotide-exchange factors. Trends Cell Biol. *10*, 60–67.

Jansen, M., Ohsaki, Y., Rega, L.R., Bittman, R., Olkkonen, V.M., and Ikonen, E. (2011). Role of ORPs in sterol transport from plasma membrane to ER and lipid droplets in mammalian cells. Traffic *12*, 218–231.

King, C., Sengupta, P., Seo, A.Y., and Lippincott-Schwartz, J. (2020). ER membranes exhibit phase behavior at sites of organelle contact. Proc. Natl. Acad. Sci. USA *117*, 7225–7235.

Klausner, R.D., Donaldson, J.G., and Lippincott-Schwartz, J. (1992). Brefeldin A: insights into the control of membrane traffic and organelle structure. J. Cell Biol. *116*, 1071–1080.

Kuehn, M.J., Herrmann, J.M., and Schekman, R. (1998). COPII-cargo interactions direct protein sorting into ER-derived transport vesicles. Nature *391*, 187–190.

Ladinsky, M.S., Mastronarde, D.N., McIntosh, J.R., Howell, K.E., and Staehelin, L.A. (1999). Golgi structure in three dimensions: functional insights from the normal rat kidney cell. J. Cell Biol. *144*, 1135–1149.

Lee, T.H., and Linstedt, A.D. (2000). Potential role for protein kinases in regulation of bidirectional endoplasmic reticulum-to-Golgi transport revealed by protein kinase inhibitor H89. Mol. Biol. Cell *11*, 2577–2590.

Lee, M.C., Miller, E.A., Goldberg, J., Orci, L., and Schekman, R. (2004). Bidirectional protein transport between the ER and Golgi. Annu. Rev. Cell Dev. Biol. *20*, 87–123.

Lingwood, D., and Simons, K. (2010). Lipid rafts as a membrane-organizing principle. Science *327*, 46–50.

Loftus, A.F., Hsieh, V.L., and Parthasarathy, R. (2012). Modulation of membrane rigidity by the human vesicle trafficking proteins Sar1A and Sar1B. Biochem. Biophys. Res. Commun. *426*, 585–589.

Long, K.R., Yamamoto, Y., Baker, A.L., Watkins, S.C., Coyne, C.B., Conway, J.F., and Aridor, M. (2010). Sar1 assembly regulates membrane constriction and ER export. J. Cell Biol. *190*, 115–128.

Lowe, D.G. (2004). Distinctive Image Features from Scale-Invariant Keypoints. Int. J. Comput. Vis. *60*, 91–110.

McCaughey, J., Stevenson, N.L., Cross, S., and Stephens, D.J. (2019). ER-to-Golgi trafficking of procollagen in the absence of large carriers. J. Cell Biol. *218*, 929–948.

Miller, E.A., Beilharz, T.H., Malkus, P.N., Lee, M.C., Hamamoto, S., Orci, L., and Schekman, R. (2003). Multiple cargo binding sites on the COPII subunit Sec24p ensure capture of diverse membrane proteins into transport vesicles. Cell *114*, 497–509.

Mironov, A.A., Mironov, A.A., Jr., Beznoussenko, G.V., Trucco, A., Lupetti, P., Smith, J.D., Geerts, W.J., Koster, A.J., Burger, K.N., Martone, M.E., et al.

(2003). ER-to-Golgi carriers arise through direct en bloc protrusion and multistage maturation of specialized ER exit domains. Dev. Cell *5*, 583–594.

Mitrovic, S., Ben-Tekaya, H., Koegler, E., Gruenberg, J., and Hauri, H.P. (2008). The cargo receptors Surf4, endoplasmic reticulum-Golgi intermediate compartment (ERGIC)-53, and p25 are required to maintain the architecture of ERGIC and Golgi. Mol. Biol. Cell *19*, 1976–1990.

Monetta, P., Slavin, I., Romero, N., and Alvarez, C. (2007). Rab1b interacts with GBF1 and modulates both ARF1 dynamics and COPI association. Mol. Biol. Cell *18*, 2400–2410.

Niu, T.K., Pfeifer, A.C., Lippincott-Schwartz, J., and Jackson, C.L. (2005). Dynamics of GBF1, a Brefeldin A-sensitive Arf1 exchange factor at the Golgi. Mol. Biol. Cell *16*, 1213–1222.

Omari, S., Makareeva, E., Roberts-Pilgrim, A., Mirigian, L., Jarnik, M., Ott, C., Lippincott-Schwartz, J., and Leikin, S. (2018). Noncanonical autophagy at ER exit sites regulates procollagen turnover. Proc. Natl. Acad. Sci. USA *115*, E10099–E10108.

Omari, S., Makareeva, E., Gorrell, L., Jarnik, M., Lippincott-Schwartz, J., and Leikin, S. (2020). Mechanisms of procollagen and HSP47 sorting during ER-to-Golgi trafficking. Matrix Biol. *93*, 79–94.

Orci, L., Stamnes, M., Ravazzola, M., Amherdt, M., Perrelet, A., Söllner, T.H., and Rothman, J.E. (1997). Bidirectional transport by distinct populations of COPI-coated vesicles. Cell *90*, 335–349.

Patterson, G.H., Hirschberg, K., Polishchuk, R.S., Gerlich, D., Phair, R.D., and Lippincott-Schwartz, J. (2008). Transport through the Golgi apparatus by rapid partitioning within a two-phase membrane system. Cell *133*, 1055–1067.

Peotter, J., Kasberg, W., Pustova, I., and Audhya, A. (2019). COPII-mediated trafficking at the ER/ERGIC interface. Traffic *20*, 491–503.

Pind, S.N., Nuoffer, C., McCaffery, J.M., Plutner, H., Davidson, H.W., Farquhar, M.G., and Balch, W.E. (1994). Rab1 and Ca2+ are required for the fusion of carrier vesicles mediating endoplasmic reticulum to Golgi transport. J. Cell Biol. *125*, 239–252.

Presley, J.F., Cole, N.B., Schroer, T.A., Hirschberg, K., Zaal, K.J., and Lippincott-Schwartz, J. (1997). ER-to-Golgi transport visualized in living cells. Nature *389*, 81–85.

Presley, J.F., Ward, T.H., Pfeifer, A.C., Siggia, E.D., Phair, R.D., and Lippincott-Schwartz, J. (2002). Dissection of COPI and Arf1 dynamics in vivo and role in Golgi membrane transport. Nature *417*, 187–193.

Raote, I., and Malhotra, V. (2019). Protein transport by vesicles and tunnels. J. Cell Biol. *218*, 737–739.

Raote, I., and Malhotra, V. (2021). Tunnels for Protein Export from the Endoplasmic Reticulum. Annu. Rev. Biochem. Published online January 27, 2021. https://doi.org/10.1146/annurev-biochem-080120-022017.

Raote, I., Ortega-Bellido, M., Santos, A.J., Foresti, O., Zhang, C., Garcia-Parajo, M.F., Campelo, F., and Malhotra, V. (2018). TANGO1 builds a machine for collagen export by recruiting and spatially organizing COPII, tethers and membranes. eLife *7*, e32723.

Ridsdale, A., Denis, M., Gougeon, P.Y., Ngsee, J.K., Presley, J.F., and Zha, X. (2006). Cholesterol is required for efficient endoplasmic reticulum-to-Golgi transport of secretory membrane proteins. Mol. Biol. Cell *17*, 1593–1605.

Rout, M.P., and Field, M.C. (2017). The Evolution of Organellar Coat Complexes and Organization of the Eukaryotic Cell. Annu. Rev. Biochem. *86*, 637–657.

Saito, K., Chen, M., Bard, F., Chen, S., Zhou, H., Woodley, D., Polischuk, R., Schekman, R., and Malhotra, V. (2009). TANGO1 facilitates cargo loading at endoplasmic reticulum exit sites. Cell *136*, 891–902.

Saraste, J., and Kuismanen, E. (1984). Pre- and post-Golgi vacuoles operate in the transport of Semliki Forest virus membrane glycoproteins to the cell surface. Cell *38*, 535–549.

Satpute-Krishnan, P., Ajinkya, M., Bhat, S., Itakura, E., Hegde, R.S., and Lippincott-Schwartz, J. (2014). ER stress-induced clearance of misfolded GPI-anchored proteins via the secretory pathway. Cell *158*, 522–533.

Scales, S.J., Pepperkok, R., and Kreis, T.E. (1997). Visualization of ER-to-Golgi transport in living cells reveals a sequential mode of action for COPII and COPI. Cell *90*, 1137–1148.

Schweizer, A., Fransen, J.A., Bächi, T., Ginsel, L., and Hauri, H.P. (1988). Identification, by a monoclonal antibody, of a 53-kD protein associated with a tubulo-vesicular compartment at the cis-side of the Golgi apparatus. J. Cell Biol. *107*, 1643–1653.

Sengupta, P., Seo, A.Y., Pasolli, H.A., Song, Y.E., Johnson, M.C., and Lippincott-Schwartz, J. (2019). A lipid-based partitioning mechanism for selective incorporation of proteins into membranes of HIV particles. Nat. Cell Biol. *21*, 452–461.

Seo, A.Y., Lau, P.W., Feliciano, D., Sengupta, P., Gros, M.A.L., Cinquin, B., Larabell, C.A., and Lippincott-Schwartz, J. (2017). AMPK and vacuole-associated Atg14p orchestrate μ-lipophagy for energy production and long-term survival under glucose starvation. eLife *6*, e21690.

Shemiakina, I.I., Ermakova, G.V., Cranfill, P.J., Baird, M.A., Evans, R.A., Souslova, E.A., Staroverov, D.B., Gorokhovatsky, A.Y., Putintseva, E.V., Gorodnicheva, T.V., et al. (2012). A monomeric red fluorescent protein with low cytotoxicity. Nat. Commun. *3*, 1204.

Shima, D.T., Scales, S.J., Kreis, T.E., and Pepperkok, R. (1999). Segregation of COPI-rich and anterograde-cargo-rich domains in endoplasmic-reticulum-to-Golgi transport complexes. Curr. Biol. *9*, 821–824.

Shomron, O., Nevo-Yassaf, I., Aviad, T., Yaffe, Y., Zahavi, E.E., Dukhovny, A., Perlson, E., Brodsky, I., Yeheskel, A., Pasmanik-Chor, M., et al. (2019). Uncoating of COPII from ER exit site membranes precedes cargo accumulation and membrane fission. bioRxiv. https://doi.org/10.1101/727107.

Simons, K., and Vaz, W.L. (2004). Model systems, lipid rafts, and cell membranes. Annu. Rev. Biophys. Biomol. Struct. *33*, 269–295.

Simunovic, M., Evergren, E., Callan-Jones, A., and Bassereau, P. (2019). Curving Cells Inside and Out: Roles of BAR Domain Proteins in Membrane Shaping and Its Cellular Implications. Annu. Rev. Cell Dev. Biol. *35*, 111–129.

Stephens, D.J., and Pepperkok, R. (2002). Imaging of procollagen transport reveals COPI-dependent cargo sorting during ER-to-Golgi transport in mammalian cells. J. Cell Sci. *115*, 1149–1160.

Stephens, D.J., Lin-Marq, N., Pagano, A., Pepperkok, R., and Paccaud, J.P. (2000). COPI-coated ER-to-Golgi transport complexes segregate from COPII in close proximity to ER exit sites. J. Cell Sci. *113*, 2177–2185.

Subramanian, A., Capalbo, A., Iyengar, N.R., Rizzo, R., di Campli, A., Di Martino, R., Lo Monte, M., Beccari, A.R., Yerudkar, A., Del Vecchio, C., et al. (2019). Auto-regulation of Secretory Flux by Sensing and Responding to the Folded Cargo Protein Load in the Endoplasmic Reticulum. Cell *176*, 1461–1476.e23.

Toulmay, A., and Prinz, W.A. (2013). Direct imaging reveals stable, micrometer-scale lipid domains that segregate proteins in live cells. J. Cell Biol. *202*, 35–44.

van Leeuwen, W., van der Krift, F., and Rabouille, C. (2018). Modulation of the secretory pathway by amino-acid starvation. J. Cell Biol. *217*, 2261–2271.

Ward, T.H., Polishchuk, R.S., Caplan, S., Hirschberg, K., and Lippincott-Schwartz, J. (2001). Maintenance of Golgi structure and function depends on the integrity of ER export. J. Cell Biol. *155*, 557–570.

Watson, P., Forster, R., Palmer, K.J., Pepperkok, R., and Stephens, D.J. (2005). Coupling of ER exit to microtubules through direct interaction of COPII with dynactin. Nat. Cell Biol. *7*, 48–55.

Westrate, L.M., Hoyer, M.J., Nash, M.J., and Voeltz, G.K. (2020). Vesicular and uncoated Rab1-dependent cargo carriers facilitate ER to Golgi transport. J. Cell Sci. *133*, jcs239814.

Xu, C.S., Hayworth, K.J., Lu, Z., Grob, P., Hassan, A.M., García-Cerdán, J.G., Niyogi, K.K., Nogales, E., Weinberg, R.J., and Hess, H.F. (2017). Enhanced FIB-SEM systems for large-volume 3D imaging. eLife *6*, e25916.

Xu, C.S., Pang, S., Shtengel, G., Müller, A., Ritter, A.T., Hoffman, H.K., Takemura, S.-y., Lu, Z., Pasolli, H.A., Iyer, N., et al. (2020). Isotropic 3D electron

microscopy reference library of whole cells and tissues. bioRxiv. https://doi.org/10.1101/2020.11.13.382457.

Zanetti, G., Pahuja, K.B., Studer, S., Shim, S., and Schekman, R. (2011). COPII and the regulation of protein sorting in mammals. Nat. Cell Biol. *14*, 20–28.

Zanetti, G., Prinz, S., Daum, S., Meister, A., Schekman, R., Bacia, K., and Briggs, J.A. (2013). The structure of the COPII transport-vesicle coat assembled on membranes. eLife *2*, e00951.

Zeuschner, D., Geerts, W.J., van Donselaar, E., Humbel, B.M., Slot, J.W., Koster, A.J., and Klumperman, J. (2006). Immuno-electron tomography of ER exit sites reveals the existence of free COPII-coated transport carriers. Nat. Cell Biol. *8*, 377–383.

Zhu, C., Das, S.L., and Baumgart, T. (2012). Nonlinear sorting, curvature generation, and crowding of endophilin N-BAR on tubular membranes. Biophys. J. *102*, 1837–1845.

STAR★METHODS

KEY RESOURCES TABLE

REAGENT or RESOURCE	SOURCE	IDENTIFIER
Antibodies		
Rabbit polyclonal anti-βCOP	Abcam	Cat# ab2899; RRID: AB_2081300
Mouse monoclonal anti-P150^{Glued}	BD Biosciences	Cat# 610474; RRID: AB_397846
Donkey-anti-Rabbit, Alexa Fluor 488	ThermoFisher	Cat# A21206; RRID:AB_2535792
Goat-anti-Rabbit, Alexa Fluor 488	ThermoFisher	Cat# A11011; RRID:AB_143157
Goat-anti-Mouse, Alexa Fluor 488	ThermoFisher	Cat# A32723; RRID: AB_2633275
Goat-anti-Mouse, Alexa Fluor 568	ThermoFisher	Cat# A11031; RRID:AB_144696
Goat-anti-Mouse, Alexa Fluor 647	ThermoFisher	Cat# A32728; RRID:AB_2633277
Bacterial strains		
DH5α	New England Biolabs	Cat# C2987H
Stable Competent *E. coli*	New England Biolabs	Cat# C3040H
Chemicals		
Biotin (working concentration: 40–80 μM)	Sigma-Aldrich	Cat# B4501
TopFluor-cholesterol	Avanti polar lipids	Cat# 810255
Methyl-β-cyclodextrin	Sigma-Aldrich	Cat# C4555
H89 (working concentration: 50 μM)	Sigma-Aldrich	Cat# B1427
Brefeldin A (BFA, working concentration: 10 μM)	Sigma-Aldrich	Cat# B7651
Normal donkey serum	Jackson ImmunoResearch Laboratories	Cat# 017-000-121
Normal goat serum	Abcam	Cat# ab7481
Paraformaldehyde	Electron Microscopy Sciences	Cat# 15710
Methanol	Fisher Chemical	Cat# A412-1
Glutaraldehyde	Electron Microscopy Sciences	Cat# 16020
Critical commercial assays		
TransIT-LT1 Transfection Reagent	Mirus	Cat# MIR 2304
Lipofectamine 2000 Transfection Reagent	ThermoFisher	Cat# 11668030
Lipofectamine 3000 Transfection Reagent	ThermoFisher	Cat# L3000008
QuickChange site-direct mutagenesis kit	Agilent	Cat# 200519
InFusion HD cloning kit	TaKaRa	Cat# 638909
Deposited data		
jrc_hela-21	Generated here	10.25378/janelia.13469550
jrc_hela-22	Generated here	10.25378/janelia.13469901
jrc_bfa	Generated here	10.25378/janelia.13469814
jrc_h89-1	Generated here	10.25378/janelia.13469964
jrc_h89-2	Generated here	10.25378/janelia.13469970
jrc_hela-1	Generated here	10.25378/janelia.13123415
jrc_hela-2	Previously published	10.25378/janelia.13114211
jrc_hela-3	Previously published	10.25378/janelia.13114244
Experimental models: cell lines		
HeLa cells	ATCC	ATCC CCL-2
U2OS	ATCC	ATCC HTB-96
COS-7	ATCC	ATCC CRL-1651
εCOP-CHO	Generated previously	(Presley et al., 2002)

(*Continued on next page*)

Continued

REAGENT or RESOURCE	SOURCE	IDENTIFIER
Oligonucleotides		
mApple ΔSbfI F	This paper	See Table S2
mApple ΔSbfI R	This paper	See Table S2
mApple into RUSH F	This paper	See Table S2
mApple into RUSH R	This paper	See Table S2
P58 backbone F	This paper	See Table S2
P58 backbone R	This paper	See Table S2
Halo into P58 F	This paper	See Table S2
Halo into P58 R	This paper	See Table S2
Sar1-N39T F	This paper	See Table S2
Sar1-N39T R	This paper	See Table S2
Sar1-H79G F	This paper	See Table S2
Sar1-H79G R	This paper	See Table S2
Recombinant DNA		
Halo-Sec23	Generated here	This manuscript
mEmerald-Sec23	Generated here	This manuscript
mCherry-Sec23	Generated here	This manuscript
Halo-Sec31	Generated here	This manuscript
mEmerald-Sec31	Generated here	This manuscript
mCherry-Sec61β	Previously published	Provided by Janelia
GFP-p58	Previously published	(Ward et al., 2001)
Halo-p58	Generated here	This manuscript
Sialyl Transferase-EGFP (SiT-EGFP)	Previously published	(Patterson et al., 2008)
Galactosyltransferase-EGFP (GalT-EGFP)	Previously published	(Cole et al., 1996)
SiT-FusionRed	Previously published	(Shemiakina et al., 2012)
Sar1b-YFP	Generated here	This manuscript
Sar1b-H79G-YFP	Generated here	This manuscript
Sar1b-mApple	Generated here	This manuscript
Sar1b-H79G-mApple	Generated here	This manuscript
Str-KDEL_TNFα-SBP-Halo (Halo-TNFα-RUSH)	Generated here	This manuscript
Str-KDEL_TNFα-SBP-mApple (mApple-TNFα-RUSH)	Generated here	This manuscript
Str-KDEL_SBP-Halo-GPI (Halo-GPI-RUSH)	Generated here	This manuscript
Str-KDEL_SBP-mApple-GPI (mApple-GPI-RUSH)	Generated here	This manuscript
Str-KDEL_TfR-SBP-Halo (Halo-TfR-RUSH)	Generated here	This manuscript
Str-KDEL_TfR-SBP-mApple (mApple-TfR-RUSH)	Generated here	This manuscript
Str-Ii_VSVG-SBP-Halo (Halo-VSVG-RUSH)	Generated here	This manuscript
Str-KDEL_SBP-mCherry-Gp135 (mCherry-Gp135-RUSH)	Previously published	(Fourriere et al., 2019)
Software and algorithms		
ImageJ (Fiji)	NIH	https://imagej.nih.gov/ij/
Amira	ThermoFisher	https://www.thermofisher.com/us/en/home/industrial/electron-microscopy/electron-microscopy-instruments-workflow-solutions/3d-visualization-analysis-software/amira-life-sciences-biomedical.html
OriginPro	OriginLab	https://www.originlab.com/
Nikon Elements	Nikon instruments	https://www.microscope.healthcare.nikon.com/products/software
ZEN Zeiss	Zeiss	https://www.zeiss.com/microscopy/int/products/microscope-software/zen.html
Graphpad Prism	Graphpad	https://www.graphpad.com/

(*Continued on next page*)

Continued

REAGENT or RESOURCE	SOURCE	IDENTIFIER
Other		
Eagle's minimal essential medium (EMEM)	ATCC	ATCC 30-2003
Dulbecco's Modified Eagle Medium (DMEM)	ThermoFisher	Cat# 1965092
Fetal bovine serum (FBS)	Corning	Cat# 35-011-CV
Dulbecco's PBS	ThermoFisher	Cat# 14190250
Fibronectin	EMD Millipore	Cat# FC010
Penicillin-streptomycin solution	Corning	Cat# 30-002-CI
L-Glutamine	Corning	Cat# 25-005-CI
Trypsin-EDTA (0.25%)	ThermoFisher	Cat# 25200056
Lab-Tek II chambered #1.5 coverglass	ThermoFisher	Cat# 155409
MatTek dishes with #1.5 coverslip	MatTek	Cat# P35G-1.5-10-C

RESOURCE AVAILABILITY

Lead contact

Further information and requests for resources and reagents should be directed to and will be fulfilled by the Lead Contact, Jennifer Lippincott-Schwartz (lippincottschwartzj@hhmi.org).

Materials availability

Plasmids generated in this study have been deposited to Addgene.

Data and code availability

FIB-SEM dataset generated in this study have been uploaded to https://openorganelle.janelia.org. See below for details.

EXPERIMENTAL MODEL AND SUBJECT DETAILS

Cell culture

HeLa, U2OS, and COS-7 cells were purchased from American Type Culture Collection (ATCC). HeLa cells were maintained in EMEM medium supplemented with 10% FBS and 1X penicillin-streptomycin solution. U2OS, COS-7, and εCOP-CHO cells were cultured in DMEM medium with 10% FBS 1 mM glutamine, and 1X penicillin-streptomycin solution. TransIT-LT1 reagent was used for transfecting HeLa cells, Lipofectamine 3000 for U2OS and COS-7 cells, and Lipofectomine 2000 for εCOP-CHO cells. Transfections were performed according to manufacturers' instructions for 16-20 hours with the following amount of DNA plasmids (per 0.7-1 cm^2 culture area): 30 ng for SiT-fluorescence protein (FP) and GalT-FP; 50 ng for FP-Sec61β, Sar1-FP, Sar1-H79G-FP, and FP-p58; 75-100 ng for FP-Sec23 and FP-Sec31; 150-200 ng for RUSH plasmids.

DNA plasmids

mCherry-Sec61β were provided by Molecular Biology Core at Janelia Research Campus. mEmerald-Sec23A, mCherry-Sec23A, and Halo-Sec23A were generated by replacing the YFP portion of YFP-Sec23A (Addgene 66611) (Stephens et al., 2000) with mEmerald, mCherry, and Halo, respectively, using AgeI and BsrGI restriction sites. Halo-Sec31 and mEmerald-Sec31 were generated by replacing the CFP portion of CFP-Sec31A (Addgene 66612) (Stephens et al., 2000) with Halo and mEmerlad, respectively, using NheI and BsrGI sites. Sar1b-YFP was generated by changing the 39th amino acid to T in Sar1b-T39N-YFP (Addgene 128155) via site-directed mutagenesis. Sar1-H79G-YFP was then created by mutating H at the 79th amino acid to T in Sar1b-YFP via site-directed mutagenesis. mApple-tagged Sar1 constructs were generated by replacing the YFP portion of Sar1 constructs with mApple using AgeI and BsrGI sites. Halo-P58 was generated via InFusion cloning kit with a Halo PCR fragment and a P58 backbone PCR fragment. To generated mApple-tagged RUSH constructs, we first created mApple-ΔSbfI-C1 vector to mutate the internal SbfI site in mApple-C1 via site-directed mutagenesis. mApple-RUSH constructs (GPI, TfR, and TNFα) were generated by replacing the EGFP portion of EGFP-GPI-RUSH, EGFP-TfR-RUSH, and EGFP-TNFα-RUSH with a PCR fragment containing mApple-ΔSbfI linked with 5′ SbfI site and 3′ FseI site. Halo-GPI-RUSH, Halo-TfR-RUSH, Halo-VSVG-RUSH, and Halo-TNFα-RUSH were generated the same way using a PCR fragment containing Halo linked with 5′ SbfI site and 3′ FseI site. All oligonucleotides used are listed in Table S2.

METHOD DETAILS

Fluorescence microscopy imaging

All cells were grown and transfected on Lab-Tek II chambered #1.5 coverglasses or MatTek dishes with #1.5 coverslip. Confocal microscopy was performed on a custom-built Nikon Eclipse Ti microscope with a YOKOGAWA CSU-X1 Spinning Disk Confocal unit using SR Apo TIRF 100x/1.49 or Plan Apo λ 60x/1.40 objectives. Airyscan imaging were performed using Plan Apo 63x/1.4 objective on ZEISS LSM 880 with Airyscan. Live-cell confocal experiments were conducted with cells incubated in phenol red-free medium at 37°C with 5% CO_2 and humidified air. Photobleaching experiments were performed on the custom-built Nikon microscope equipped with Bruker photoactivation module. HeLa cells co-expressing mEmerald-Sec23 and Halo-TNFα-RUSH stained with JF640 Halo-ligand were subjected to 640 nm laser pulse at maximal intensity in 3.14-μm^2 circular areas to photobleach TNFα-RUSH at ERESs and imaged at 488 nm and 640 nm to monitor the fluorescence recovery. For synchronized cargo release experiments, HeLa or εCOP-CHO cells transfected with RUSH cargo were incubated with biotin at a final concentration of 80 μM.

Cell fixation and immunostaining

All procedures were performed at room temperature and all washing steps were done by DPBS for 5 min unless otherwise indicated. For βCOP immunostaining, cells were rinsed with DPBS and fixed with 4% paraformaldehyde and 0.1% glutaraldehyde in DPBS for 20 min. Fixed cells were quenched with 100 mM glycine in DPBS, washed twice, and permeabilized by 0.3% Triton X-100 in DPBS for 20 min. For $p150^{Glued}$ immunostaining and $p150^{Glued}$ co-immunostaining with βCOP, cells were fixed with methanol (pre-chilled to −20°C) at −20°C for 5 min. Fixed cells were then washed with DPBS followed by 20 μM digitonin permeabilization in DPBS for 20 min. Permeabilized cells, either by Triton X-100 or digitonin, were then blocked with 5% normal donkey or goat serum in DPBS for 1 h followed by incubation with primary antibody (anti-βCOP antibody, 1:200 dilution; anti-$p150^{Glued}$ antibody, 1:500 dilution) in DPBS with 1% BSA at 4°C overnight. After three washes, the samples were incubated with fluorescent secondary antibody (1: 2,000 in dilution) for 1 h. The stained samples were washed for three times and imaged with confocal or Airyscan microscopy at room temperature.

TopFluor-cholesterol labeling

TopFluor-cholesterol was mixed with methyl-β-cyclodextrin (MβCD) as previously described (Jansen et al., 2011). In brief, TopFluor-cholesterol was dissolved in choloroform:methanol 1:1 (v:v) at a concentration of 1 mg/ml in a glass tube. The solution was then dried under a stream of argon gas followed by the addition of 370 mM MβCD in PBS in a 100:1 molar ratio to TopFluor-cholesterol. This mixture was then vortexed, sonicated in water bath for 1-3 min, and incubated at 37°C avoiding light for overnight on a rocker. Undissolved TopFluor-cholesterol was removed by centrifugation at 16,000 x g for 15 min. The supernatant containing TopFluor-cholesterol/MβCD mix was aliquoted and stored at −30°C. To monitor subcellular distribution of cholesterol, transfected HeLa cells were incubated with TopFluor-cholesterol/MβCD mix in 1:2,000 dilution for 5 min. Cells were then incubated in label-free media for 30 min to 1 h allowing TopFluor-cholesterol at the PM to be internalized and to reach cholesterol-rich membranes/organelles prior to imaging experiments.

Cryo-SIM/FIB-SEM and analysis

Cryo-SIM, EM sample preparation, and FIB-SEM imaging was performed as previously described (Hoffman et al., 2020; Xu et al., 2017, 2020). In short, the cells plated on sapphire coverslips were high-pressure frozen and then optically imaged in the custom optical cryostat. SIM images were processed as described (Gustafsson et al., 2008). Following optical imaging, samples were freeze-substituted and resin-embedded. Regions of interested were identified using an XRadia 510 Versa micro X-Ray system (Carl Zeiss X-ray Microscopy Inc.) and then trimmed to expose small (~100 μm × 100 μm × 60 μm) tabs. FIB-SEM datasets were generated using a Zeiss Capella FIB column fitted onto a Zeiss Merlin SEM for 8 nm isotropic voxels and a Zeiss Gemini500 SEM for 4nm isotropic voxels. The final datasets were registered using a SIFT-based algorithm (Lowe, 2004). To register the FIB-SEM to cryo-SIM we used the software package BigWarp (Bogovic et al., 2016) and morphological ER landmarks as described (Hoffman et al., 2020). All segmentation was performed using semi-manual thresholding and manual painting tools within Amira (Thermo Fisher Scientific). 3D rendered images and movies were created within Amira. Below is a brief description for each sample including cell type, general sample preparation details, and original publication (where applicable).

jrc_hela-21

Sample: Interphase HeLa cell overexpressing mApple-TNFa-RUSH, frozen 8 min post 50 μM biotin addition.
Protocol: High pressure freezing, freeze-substitution resin embedding with 1% OsO4 0.1% UA 3% H2O in acetone; resin embedding in Eponate 12.
Contributions: Sample provided by Aubrey Weigel (HHMI/Janelia), prepared for imaging by Gleb Shtengel (HHMI/Janelia), with imaging and post-processing by C. Shan Xu (HHMI/Janelia).
Voxel size: 8 nm × 8 nm × 8 nm
Dimensions: 50 μm x 10 μm x 15.58 μm
Acquisition date: 2017-04-12

OpenOrganelle link: https://openorganelle.janelia.org/datasets/jrc_hela-21
https://doi.org/10.25378/janelia.13469550

jrc_hela-22

Sample: Interphase HeLa cell overexpressing mApple-TNFa-RUSH, frozen 8 min post 50 μM biotin addition.
Protocol: High pressure freezing, freeze-substitution resin embedding with 1% OsO4 0.1% UA 3% H2O in acetone; resin embedding in Eponate 12.
Contributions: Sample provided by Aubrey Weigel (HHMI/Janelia), prepared for imaging by Gleb Shtengel (HHMI/Janelia), with imaging and post-processing by C. Shan Xu (HHMI/Janelia).
Voxel size: 8 nm × 8 nm × 8 nm
Dimensions (μm): 8 3.36 μm x 8.46 μm x 33 μm
Acquisition date: 2017-04-12
OpenOrganelle link: https://openorganelle.janelia.org/datasets/jrc_hela-22
https://doi.org/10.25378/janelia.13469901

jrc_hela-bfa

Sample: Interphase HeLa cell overexpressing mEmerald-Sec23 frozen 6 min post 10 μM BFA addition.
Protocol: High pressure freezing, freeze-substitution resin embedding with 1% OsO4 0.1% UA 3% H2O in acetone; resin embedding in Eponate 12.
Contributions: Sample provided by Aubrey Weigel and Chi-Lun Chang (HHMI/Janelia), prepared for imaging by Gleb Shtengel (HHMI/Janelia) and Melanie Freeman (UC Berkeley), with imaging and post-processing by C. Shan Xu (HHMI/Janelia).
Voxel size: 8 nm × 8 nm × 8 nm
Dimensions: 65 μm x 4.8 μm x 51.6 μm
Acquisition date: 2019-10-15
OpenOrganelle link: https://openorganelle.janelia.org/datasets/jrc_hela-bfa
https://doi.org/10.25378/janelia.13469814

jrc_hela-h89-1

Sample: Interphase HeLa cell overexpressing mEmerald-Sec23 frozen 9 min post 50 μM H89 addition.
Protocol: High pressure freezing, freeze-substitution resin embedding with 1% OsO4 0.1% UA 3% H2O in acetone; resin embedding in Eponate 12.
Contributions: Sample provided by Aubrey Weigel and Chi-Lun Chang (HHMI/Janelia), prepared for imaging by Gleb Shtengel (HHMI/Janelia), with imaging and post-processing by C. Shan Xu (HHMI/Janelia).
Voxel size: 8 nm × 8 nm × 8 nm
Dimensions: 80 μm x 6 μm x 101.82 μm
Acquisition date: 2020-10-09
OpenOrganelle link: https://openorganelle.janelia.org/datasets/jrc_hela-h89-1

jrc_hela-h89-2

Sample: Interphase HeLa cell overexpressing mEmerald-Sec23 frozen 9 min post 50 μM H89 addition.
Protocol: High pressure freezing, freeze-substitution resin embedding with 1% OsO4 0.1% UA 3% H2O in acetone; resin embedding in Eponate 12.
Contributions: Sample provided by Aubrey Weigel and Chi-Lun Chang (HHMI/Janelia), prepared for imaging by Gleb Shtengel (HHMI/Janelia), with imaging and post-processing by C. Shan Xu (HHMI/Janelia).
Voxel size: 8 nm × 8 nm × 8 nm
Dimensions: 50 × 8 x 98.86 (X, Y, Z)
Acquisition date: 2020-10-15
OpenOrganelle link: https://openorganelle.janelia.org/datasets/jrc_hela-h89-2
https://doi.org/10.25378/janelia.13469964

jrc_hela-1

Sample: Wild-type, interphase HeLa cell (ATCC CCL-2).
Protocol: High pressure freezing, freeze-substitution resin embedding with 2% OsO4 0.1% UA 3% H2O in acetone; resin embedding in Eponate 12.

Contributions: Sample provided by Aubrey Weigel (HHMI/Janelia), prepared for imaging by Gleb Shtengel (HHMI/Janelia), with imaging and post-processing by C. Shan Xu (HHMI/Janelia).
Voxel size: 8 nm × 8 nm × 8 nm
Dimensions: 75 μm x 8 μm x 60 μm
Acquisition date: 2017-04-05
OpenOrganelle link: https://www.openorganelle.com/datasets/jrc_hela-1
https://doi.org/10.25378/janelia.13123415

jrc_hela-2

Sample: Wild-type, interphase HeLa cell (ATCC CCL-2).
Protocol: High pressure freezing, freeze-substitution resin embedding with 2% OsO4 0.1% UA 3% H2O in acetone; resin embedding in Eponate 12.
Contributions: Sample provided by Aubrey Weigel (HHMI/Janelia), prepared for imaging by Gleb Shtengel (HHMI/Janelia), with imaging and post-processing by C. Shan Xu (HHMI/Janelia).
Voxel size: 4 nm × 4 nm × 5.24 nm
Dimensions: 48 μm x 6 μm x 33 μm
Acquisition date: 2017-06-21
OpenOrganelle link: https://www.openorganelle.com/datasets/jrc_hela-2
https://doi.org/10.25378/janelia.13114211
Publication: (Xu et al., 2020)

jrc_hela-3

Sample: Wild-type, interphase HeLa cell (ATCC CCL-2).
Protocol: High pressure freezing, freeze-substitution resin embedding with 2% OsO4 0.1% UA 3% H2O in acetone; resin embedding in Eponate 12.
Contributions: Sample provided by Aubrey Weigel (HHMI/Janelia), prepared for imaging by Gleb Shtengel (HHMI/Janelia), with imaging and post-processing by C. Shan Xu (HHMI/Janelia).
Voxel size: 4 nm × 4 nm × 5.24 nm
Dimensions: 50 μm x 4 μm x 39 μm
Acquisition date: 2017-08-9
OpenOrganelle link: https://www.openorganelle.com/datasets/jrc_hela-3
https://doi.org/10.25378/janelia.13114244
Publication: (Xu et al., 2020)

QUANTIFICATION AND STATISTICAL ANALYSIS

Image analysis

All image analyses were performed using ImageJ (National Institutes of Health) unless otherwise indicated. All intensity analyses were subjected to background subtraction. To obtain relative intensity profiles, the intensity values from different conditions were normalized to that at the first time point or in control groups. Diameters of ERES, comprising tubules, ER, ER-ERES necks, and transport intermediates were measured by finding the peak-to-peak distance of line-profile cross-sections from FIB-SEM slices. Distribution of COPI with respect to ERES was quantified by measuring the percentage pixels occupied by both COPI and COPII fluorescence after thresholding. For separation analysis, intensity profiles of corresponding fluorescence puncta were fit to a Gaussian curve to determine its center position. Separation distances are reported relative to the center distance of COPII puncta. Temporal projection maps were generated by Temporal-Color Code from stacks of time-lapse images in ImageJ. COPII, COPI, and RUSH cargo tracking was manually done using Tracking Plugin in ImageJ. To evaluate the % volume occupied by vesicles near and away from ERES, vesicles and cytosol in one cubic micron ROIs were manually segmented. The reported numbers are the ratio of the volume occupied by vesicles versus the total available cytosolic volume.

Statistical analysis

Data were statistically analyzed by two-tailed t test or one-way ANOVA with Tukey's multiple comparisons using GraphPad Prism (GraphPad Software; La Jolla, CA). Data distribution assumed to be normal but not formally tested. *, $p < 0.05$; ** $p < 0.01$; ***, $p < 0.001$; n.s., not significant. Graphs were generated using OriginPro (OriginLab; Northampton, MA) and GraphPad Prism.

CellPress

Supplemental figures

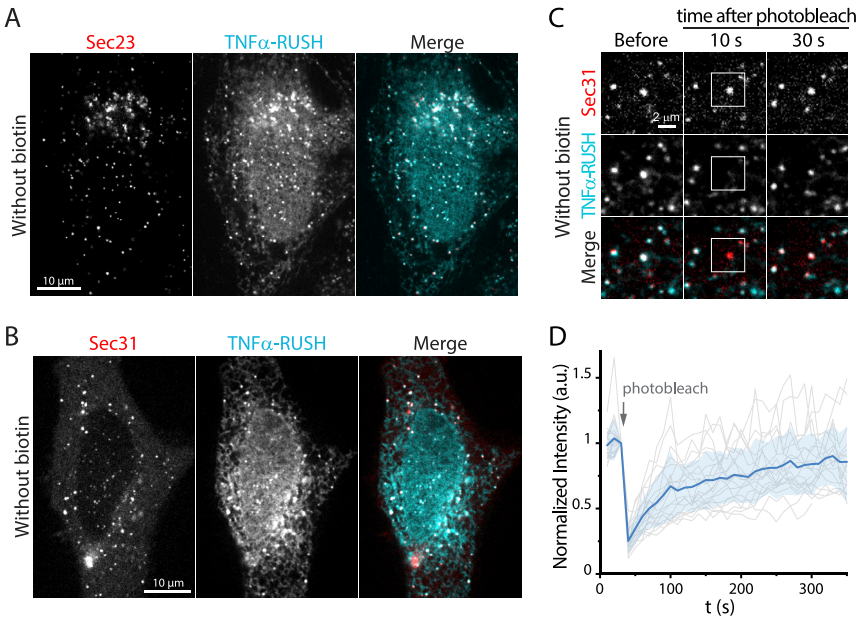

Figure S1. Distribution of TNF-α-RUSH and TopFluor-cholesterol in steady-state HeLa cells, related to Figure 1

(A and B) Steady-state distribution of TNFα-RUSH at ERESs labeled by mEmerald-Sec23 (A) or by mEmerald-Sec31 (B) without biotin addition in HeLa cells monitored by confocal microscopy. Representative images are shown.

(C) Fluorescence recovery after photobleaching (FRAP) of Halo-TNFα-RUSH in a ERES labeled with mEmerald-Sec31 without biotin addition in a HeLa cell monitored by confocal microscopy. Representative images are shown.

(D) FRAP analysis of experiment described in (C). Mean (blue line) from 20 regions in three independent experiments (gray lines) and standard deviation (shaded blue) are shown.

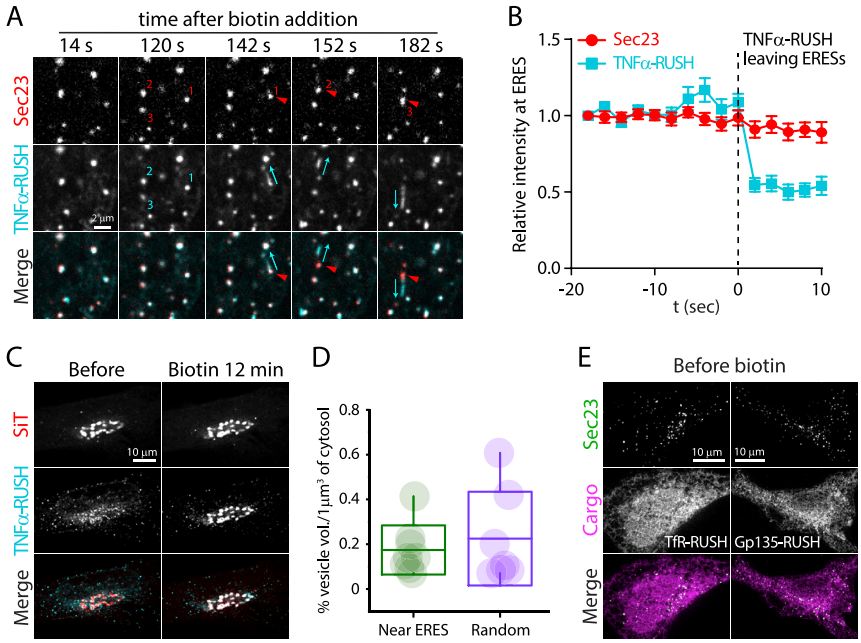

Figure S2. Dynamic distribution of RUSH cargos, related to Figure 2

(A) Halo-TNFα-RUSH transport intermediates leave from mEmerald-Sec23-labeled ERESs after the addition of biotin in HeLa cells monitored by confocal microscopy. Red arrowheads point to examples where ERESs with TNFα-RUSH cargo undergo departure from these sites, with cyan arrows showing the departure path. Representative images are shown.

(B) Quantification of TNFα-RUSH intensity within a single ERESs before and during cargo departure from the ERES from the experiment described in A. Time of TNFα-RUSH leaving ERESs is offset to t = 0. Mean ± SEM (14 ERESs) are shown.

(C) Halo-TNFα-RUSH begins colocalizing with the Golgi labeled by SiT-FusionRed within 12 min of biotin treatment. Representative images are shown.

(D) Quantification of vesicle volume near and away from an ERES analyzed from our FIB-SEM dataset. The volume occupied by vesicles within a cubic micron of available cytosol is reported. Raw data distribution and mean ± standard deviation and min-max range are shown. Results detailed in Table S1.

(E) Distribution of mApple-TfR-RUSH (left panel) and mCherry-Gp135-RUSH (right panel) before biotin addition in HeLa cells transfected with mEmerald-Sec23 monitored by confocal microscopy. Representative images are shown.

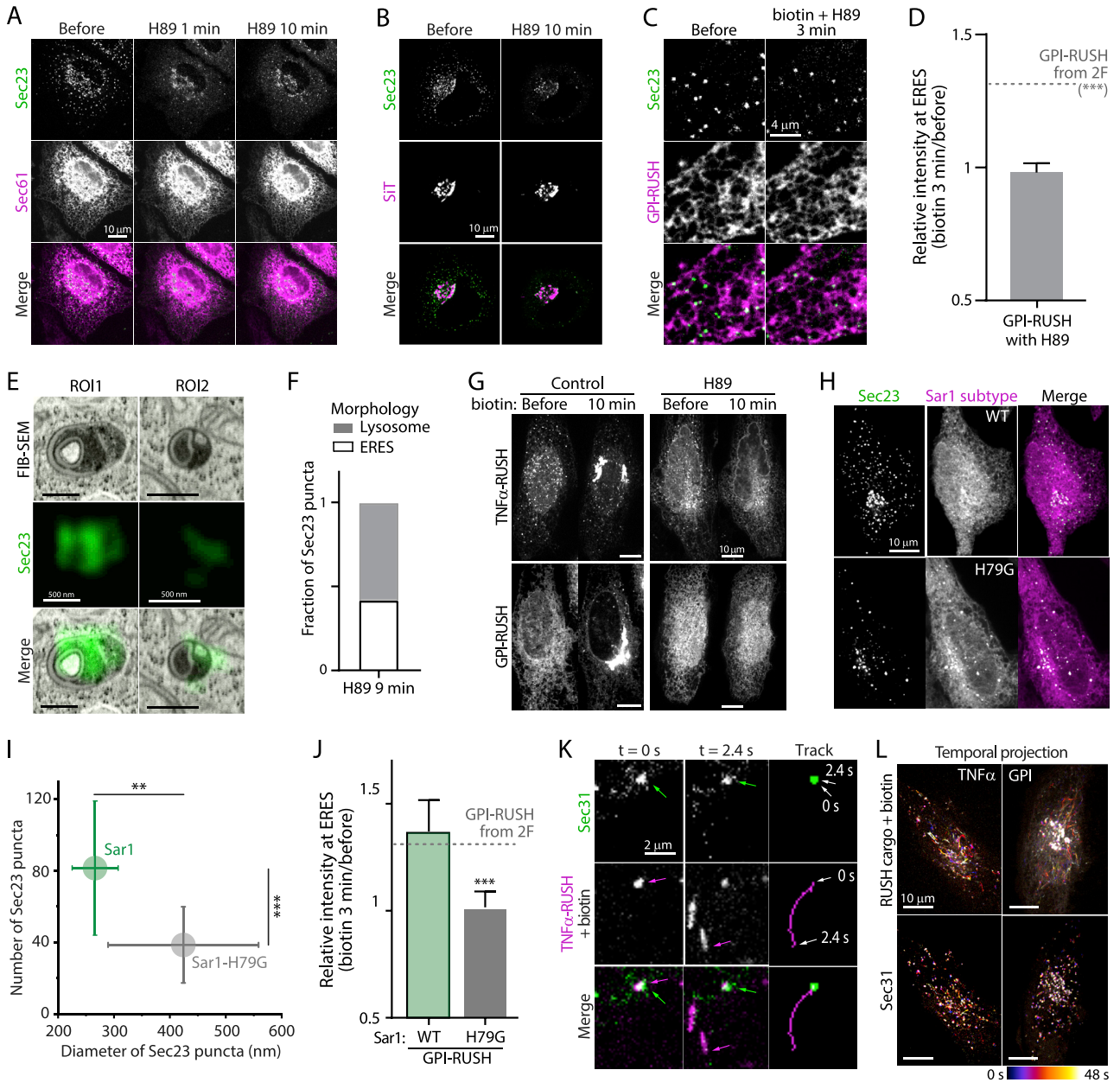

Figure S3. The effects of dynamic assembly of Sar1 on ERESs and RUSH cargo release, related to Figure 3

(A and B) 50 μM H89 treatment has minimal effect on ER labeled by mCherry-Sec61 (A) and the Golgi labeled by SiT-FusionRed (B) in HeLa cells monitored by confocal microscopy. Representative images are shown.

(C) GPI-RUSH remains in the ER after biotin addition when HeLa cells are treated with 50 μM H89 treatment for 3 min. HeLa cells were co-transfected with mEmerald-Sec23 and Halo-GPI-RUSH and monitored by confocal microscopy. Representative images are shown.

(D) Relative intensity of GPI-RUSH at ERES during H89 treatment, as described in C. Mean ± SD are shown (20 cells from three independent experiments). See also Table S1.

(E) mEmerald-Sec23 remnants with lysosome-like morphology after 9-min of H89 treatment. Representative FIB-SEM slices containing Sec23-positive lysosomal structure are shown.

(F) Fraction of Sec23 puncta with ERES or lysosome morphology as revealed by FIB-SEM in HeLa cells frozen at 9-min of H89 treatment. 200 Sec23 puncta from 2 HeLa cells were examined.

(G) RUSH cargo distribution during biotin incubation in control or H89-treated HeLa cells monitored by confocal microscopy. Representative images are shown.

(H) Distribution of mEmerald-Sec23 in fixed HeLa cells co-transfected with wild-type Sar1-mApple or Sar1-H79G-mApple monitored by Airyscan microscopy. Representative images are shown.

(I) Quantification of the number and size of Sec23 puncta as described in (H). Mean ± SD are shown. See also Table S1. **p > 0.01; ***p > 0.001.

(legend continued on next page)

(J) Relative intensity of GPI-RUSH at ERESs 3 min after biotin addition in HeLa cells overexpressing Sar1 or Sar1-H79G. Mean ± SD are shown (19-23 cells from three independent experiments). See also Table S1.

(K) TNFα-RUSH cargo leaving ERES labeled by Halo-Sec31 during biotin incubation monitored by continuous confocal imaging. Trajectory of individual Sec31 puncta (green) and TNFα-RUSH (pink) is shown for clarity, revealing that Sec31 remains at ERES while TNFα-RUSH moves away from this site. Representative images are shown.

(L) Temporal projections over 48 s of RUSH cargos (top) and ERESs labeled by Sec31 (bottom) during biotin release monitored by continuous confocal imaging. Representative images are shown.

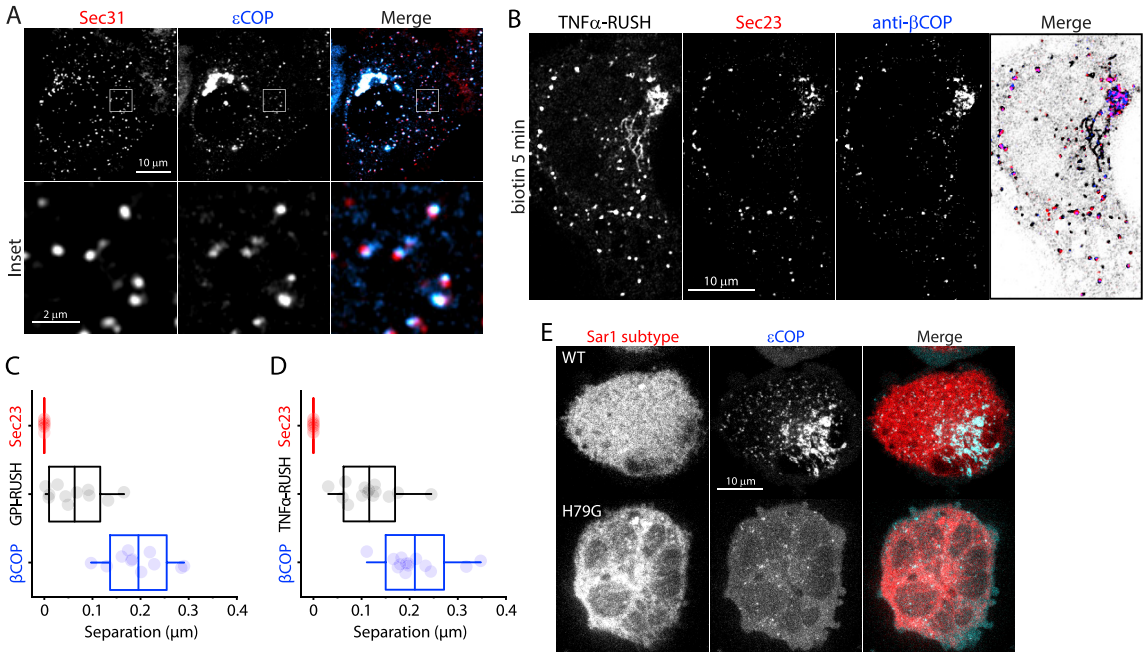

Figure S4. Distribution of COPII, COPI, or RUSH cargos in steady-state, in biotin release, or under Sar1 subtype overexpression, related to Figure 4

(A) Colocalization of Halo-Sec31 and εCOP-YFP in fixed εCOP-CHO monitored by Airyscan microscopy. Representative images are shown.

(B) Colocalization of mCherry-Sec23, Halo-TNFα-RUSH and immunostained βCOP in HeLa cells fixed at 5-min of biotin addition monitored by Airyscan microscopy. Representative images are shown.

(C and D) Separation between Sec23, GPI-RUSH (C) and TNFα-RUSH (D), and βCOP during cargo release. Raw data and mean ± standard deviation and min-max range are shown. Results detailed in Table S1.

(E) Distribution of εCOP-YFP in εCOP-CHO cells co-transfected with Sar1-mApple or Sar1-H79G-mApple monitored by confocal microscopy. Representative images are shown.

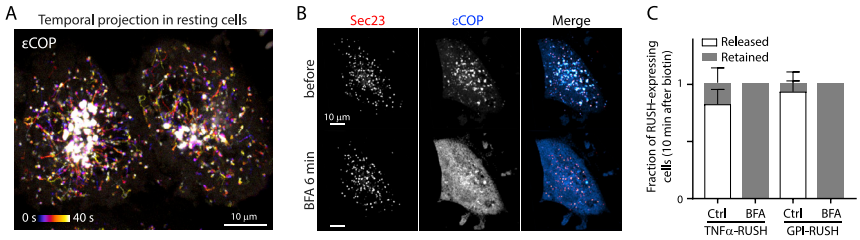

Figure S5. Dynamic distribution of εCOP-YFP and the effects of BFA on ERESs and RUSH cargo release, related to Figure 5.

(A) Temporal projection over 40 s of εCOP in εCOP-CHO cells monitored by continuous confocal imaging.

(B) Halo-Sec23 remains at ERESs while εCOP redistributes into cytosol after BFA treatment in εCOP-CHO cells monitored by confocal microscopy. Representative images are shown.

(C) Fraction of cells with RUSH cargo released or retained after 10-min of biotin treatment. Mean ± SD are shown (4 independent experiments). See also Table S1.

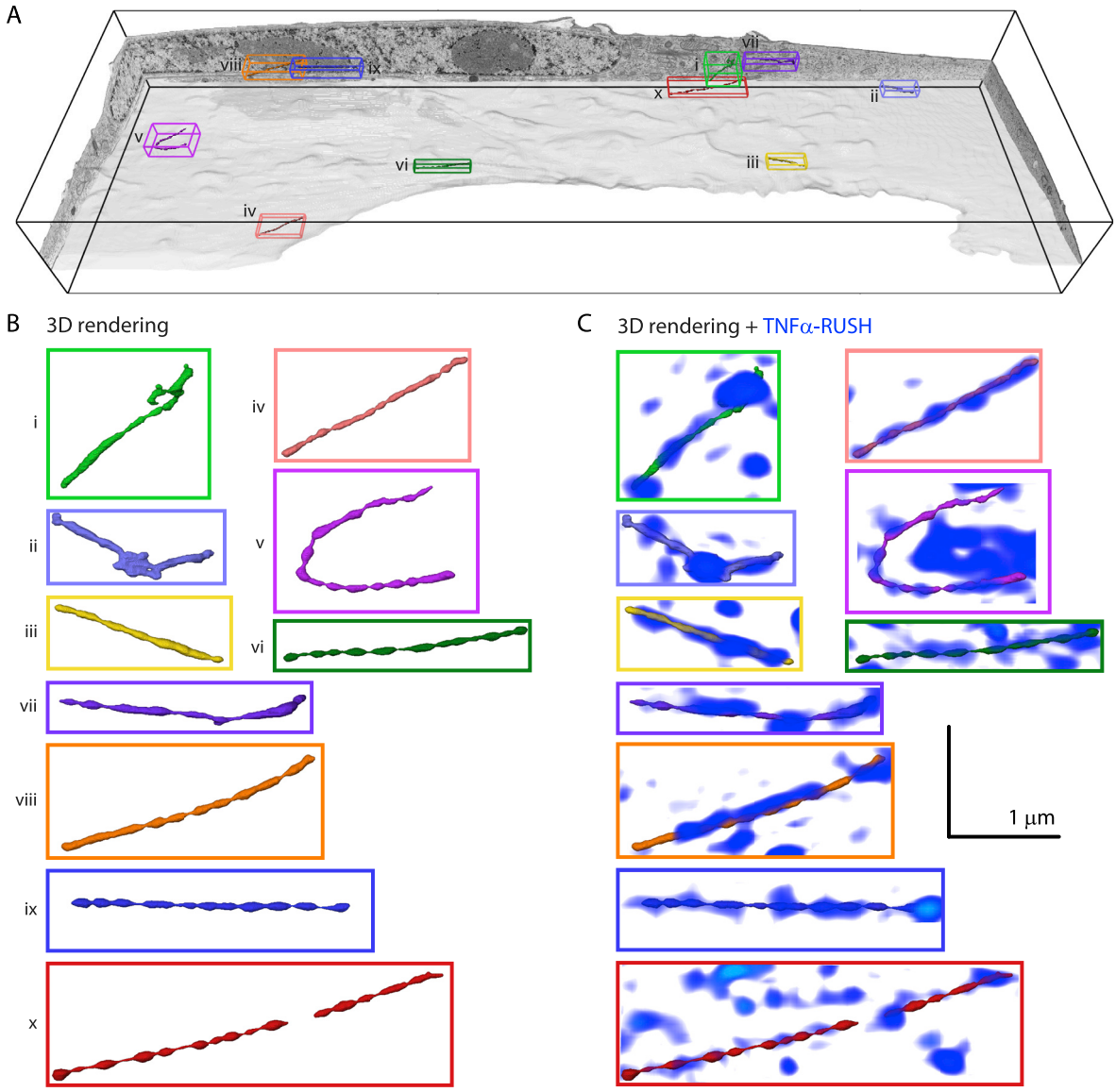

(legend on next page)

Figure S6. Profile of transport intermediates containing TNF-α-RUSH and colocalization of GPI-RUSH transport intermediate and p150^{Glued}, related to Figure 6

(A) Segmentation and 3D rendering of 10 transport intermediates shown in Figure 6.

(B-C) 3D volume rendering of transport intermediates either with (C) and without (B) TNFα-RUSH cryo-SIM are shown for each inset marked by a roman numeral in (A).

(D) Colocalization of transport intermediates and dynein microtubule motors in fixed HeLa cells overexpressing RUSH cargos and immunostained with p150^{Glued}, monitored by Airyscan microscopy. Representative images are shown.

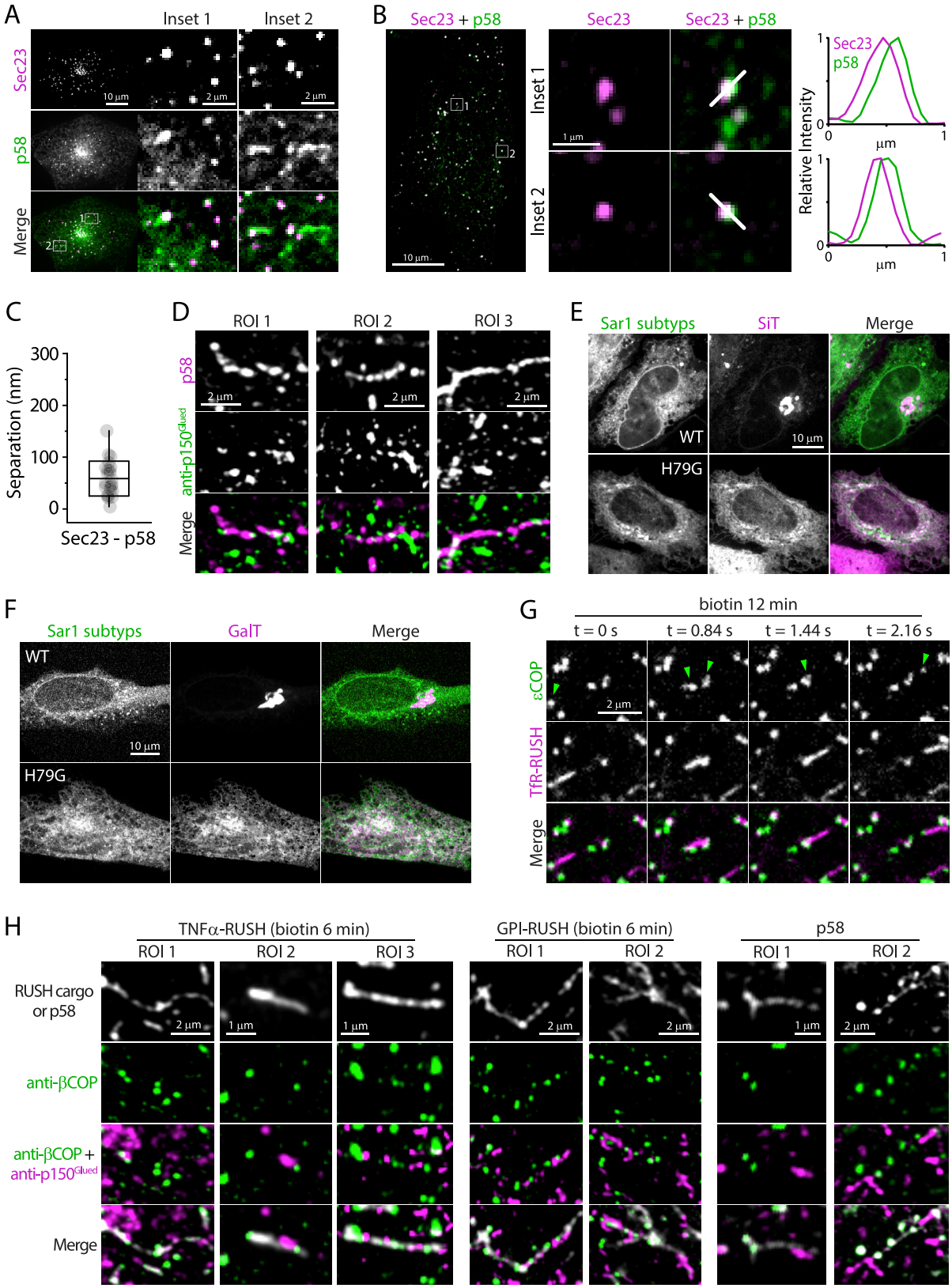

(legend on next page)

Figure S7. Distribution of p58 relative to Sec23, the effects of Sar1 subtypes on the Golgi, and COPI foci on transport intermediate, related to Figure 7

(A and B) Colocalization of Halo-Sec23 and GFP-p58 in HeLa cells monitored by confocal (A) and Airyscan (B) microscopy. Representative images and relative intensity profile (right) are shown.

(C) Separation between Sec23 and p58 at ERESs in HeLa cells as described in (B). Raw data and mean ± standard deviation and min-max range are shown. Results detailed in Table S1.

(D) Colocalization Halo-p58-positive tubes and $p150^{Glued}$ in fixed HeLa cells monitored by Airyscan microscopy. Representative images are shown.

(E and F) Sar1-H79G overexpression redistributes Golgi markers, SiT-FusionRed (E) and GalT-EGFP (F), to the ER in HeLa cells monitored by confocal microscopy. Representative images are shown.

(G) Punctate distribution of εCOP-YFP on mobile transport intermediates containing TfR-RUSH during biotin release in εCOP-CHO cells. Green arrow heads indicate εCOP-YFP foci on transport intermediates. Representative confocal images are shown.

(H) Endogenous βCOP and $p150^{Glued}$ foci on transport intermediates containing Halo-TNFα-RUSH or Halo-GPI-RUSH and Halo-p58-positive tubes in HeLa cells monitored by Airyscan microscopy. Representative confocal images are shown.